MODELING OF NON-EQUILIBRIUM PLASMAS IN AN INDUCTIVELY COUPLED PLASMA FACILITY

BY

WENBO ZHANG

THESIS

Submitted in partial fulfillment of the requirements
for the degree of Master of Science in Aerospace Engineering
in the Graduate College of the
University of Illinois at Urbana-Champaign, 2014

Urbana, Illinois

Adviser:

Professor Marco Panesi (Adviser)
Professor Huck B. Chew (Co-adviser)

Abstract

This work presents the results of the numerical simulation of ionized gas flows inside the torch of an inductively coupled plasma facility in the von Karman Institute for Fluid Dynamics. The main purpose of this work is the parametric investigation of thermo-chemical non-equilibrium effects on the plasma jet at different operating pressures ranging from 3 to 15 kPa. The test gas is an ionized air mixture represented by eleven species. The induced electric field inside the torch is computed by solving Helmholtz induction equation. The non-equilibrium effects are modeled using a standard two-temperature formulation. In particular, the present analysis assesses the impact of different chemical kinetics models and vibration-chemistry-vibration coupling models on the resulting flow and electro-magnetic fields. Results of the present work are compared with solutions previously computed by assuming local thermodynamic equilibrium (LTE)conditions and significant differences on both the induced electric and temperature field are observed especially for the low pressure cases.

To my parents

Acknowledgments

I am honored to have the opportunity to work with excellent researchers throughout my masters study. Many people have contributed directly and indirectly to this thesis and it is difficult to list them all. Firstly I would like to thank my masters advisor, Dr. Marco Panesi for his guidance and support during my masters program. I am fortunate to be introduced to the world of hypersonic flow modeling by Dr. Andrea Lani whose critical comments and technical support are essential for the completement of this thesis. I would like to thank Dr. Alessandro Munafo and my labmates, Amal Sahai, Robyn McDonald, Andrea Alberti, Shrutakeerti Mallikarjun Vagishwari for their moral support. Special thanks are given to Kevin Heritier, whose selfless help can never be ignored. Finally, I would like to thank my parents for their support and understanding throughout my whole life.

Table of Contents

List of Figures

Chapter 1

Introduction

1.1 Introduction

The atmospheric re-entry of hypersonic vehicles often generates a weakly ionized plasma surrounding the spacecraft. Formation of the plasma is due to the development of a strong shock wave which forms upstream of the vehicle, as it plunges into the lower and more dense layers of the atmosphere. Across the shock wave, the temperature rises by several thousands of degrees Kelvin. This leads to excitation of the internal energy modes, dissociation, as well as ionization of the particles.

Inductively coupled plasma (ICP) facilities (Figure 1.1) have been developed to reproduce, at least partially, the environment encountered by space vehicles during atmospheric (re-)entry. A mixture of cold gases, representative of the planetary atmosphere (*e.g.*, air, in the case of Earth entry), is injected into a solenoidal water-cooled inductor, referred to as a plasma torch. Within the torch, the gas is subjected to intense electric currents which increase its temperature via Joule heating.The aim of this work is to model the plasma flow in the ICP torch and in the post-discharge jet.

The new numerical analysis performed allows for the assessment of one of the basic assumption in the Institute for Problems in Mechanics (IPM) methodology [21, 20, 19, 22]. This approach (used to estimate the catalytic properties of thermal protection system materials) supposes in fact thermochemical equilibrium conditions to be established in the torch and in the test chamber. However, there is no proof in the literature that equilibrium [5] conditions exist and a detailed analysis

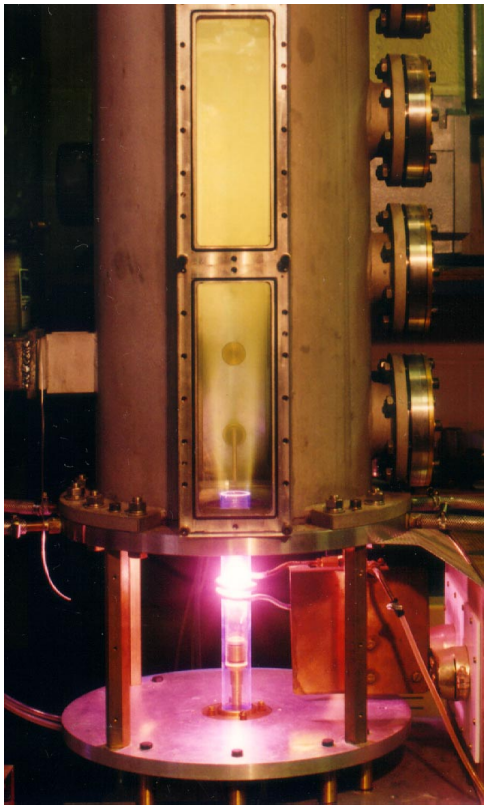

Figure 1.1: Von Karman Institute Mini Torch Plasmatron.

assessing the quality of this assumption is not available.

The plasma flow under consideration is *un-magnetized*. Thus, the thermal motion of the charged particles is governed by inter-particle collisions, and thus the magnetic field has a negligible effect. The plasma frequency is so high ($\approx 10^{11}$ Hz at $p = 0.01$ atm) that the electromagnetic waves are quickly absorbed and can be neglected from the description of the system. Significant violations of charge neutrality only occur at length scales smaller than the Debye length ($\approx 10^{-6}$ m at $p = 0.01$ atm). In the case of charge separation, the electrostatic field pulls electrons and ions together, thereby restoring the charge-neutrality of the gas. The plasma is therefore considered *quasi-neutral*. In the present work, we use the elegant formulation of the time-averaged axisymmetric magneto-hydrodynamic (MHD) equations developed by Boulos [4], Mostaghimi *et al.* [35], and McKelliget

[34].

A multi-temperature model is used to account for the non-equilibrium effects inside the torch. Thus, the population of each internal (rotational, vibrational, or electronic) energy mode is described by a Maxwell-Boltzmann distribution at a specific temperature (rotational T_r, vibrational T_v, or electronic temperature T_e). To calculate these temperatures and the energy exchanged among all the energy modes (i.e., translational, rotational, vibrational, and electronic), conservation equations for the internal energy modes under thermal non-equilibrium are added to the classical set of conservation equations for mass, momentum, and total energy.

The energy transfer inside the torch is due to the coupling of the electric field and the motion of free electrons (and, to a lesser extent, the motion of ions). Free-electrons, heated by the radio-frequency electric field, quickly transfer their energy to the electronic and vibrational energy modes. Thus, assuming instantaneous energy accommodation among these internal energy modes, a common temperature, T_{ve}, can be used to describe the population of the levels within these three energy modes. The energy transfer to the rotational and translational energy modes of heavy particles is less efficient. This transfer takes place through both inelastic vibration-translation energy transfer as well as elastic collisions of heavy and light particles. Assuming fast equilibration of rotational and translational energies, a single temperature, T_h, is used to describe the population of these two modes.

1.2 Thesis Organization

The thesis is arranged as follows: Chapter 2 presents, discusses the plasma torch configuration and the electromagnetic / fluid / thermo-chemical aspects of the ICP model, including its underlying assumptions; the numerical method is briefly described in Chapter 3; the obtained results are discussed in details in Chapter 4; finally, conclusions and future work are presented in Chapter 5.

Chapter 2

Physical Model

The mathematical model of high-pressure Inductively Coupled Plasmas is obtained by coupling Maxwell equations describing the electro-magnetic fields which excite and sustain the plasma and Boltzmann's equation the successive moments of which yields the hydrodynamic equations, namely, the species equation for each chemical component, momentum equation and energy equations. The coupling of the two sets of equations is ensured by the presence of electrical conductivity in the MHD governing equations (body forces and Joule heating term on the flow side).

The closure of the set of governing equations requires an expression for the thermodynamic and transport properties. The transport fluxes (viscous, heat conductive and diffusive) are obtained by evaluating the integrals of the particle distribution functions over velocity using the Chapman and Enskog method. The description of gas mixtures composed of species of disparate masses is well established. The extension of CE method to partially ionized plasmas is discussed by [1, 30].

A two-temperature model is used to take into account the thermal-nonequilibrium effects:

- The rotational states are equilibrated with the heavy particle translational energies at a common translational-rotational temperature T_{hr};
- The heavy particles' electronic energies and the molecular species' vibrational energies are fully equilibrated with the electron translational energies at a common electro-vibrational temperature T_{ev}.

This chapter is organized in the following manner: Sec. 2.1 describes the governing Magneto-hydrodynamics equations without taking into account contributions from internal degrees of freedom; the same set of governing equations is revisited in Sec. 2.2, where the excitation of the internal

energy modes is accounted for; the transport properties are discussed in Sec. 2.3; finally thermo-chemical models are discussed in Sec. 2.4

2.1 Governing Magneto-Hydrodynamics Equations

2.1.1 Hydrodynamics Conservation Equations

As the first step toward the mathematical modeling of high-pressure plasmas, we derive the hydrodynamics conservation equations based on a simplified representation of ionized gas mixtures by disregarding the internal degrees of freedom of the ionized gas mixture, namely, neglecting the effects of discrete quantum states of the gas particles. We represent the distribution of $s-particles$ with the distribution function $f_s(\overrightarrow{r_s}, \overrightarrow{w_s})$ in the phase space $(d\overrightarrow{r_s}, d\overrightarrow{w_s})$, which satisfies the Boltzmann's equation:

$$\frac{\partial f_s}{\partial t} + \overrightarrow{w_s} \cdot \bigtriangledown f_s + \frac{1}{m_s}\overrightarrow{F_s} \cdot \bigtriangledown_{\overrightarrow{w_s}} f_s = \left[\frac{\partial f_s}{\partial t}\right]_{el} + \left[\frac{\partial f_s}{\partial t}\right]_{ch} \tag{2.1}$$

where $\overrightarrow{F_s}$ denotes the Lorentz-force on the s-particles and the two terms on the right hand side denote the net production of particles due to elastic and inelastic collisions respectively. The hydrodynamic conservation equations, namely, the conservation equations of mass, momentum and energy, are acquired by taking successive moments of the Boltzmann equation (Eq.2.1). The microscopic governing equations are obtained by multiplying Eq.2.1 by θ_s and integrating over $\overrightarrow{w_s}$:

$$\frac{\partial}{\partial t}(n_s \langle\theta\rangle_s) + \bigtriangledown \cdot (n_s \langle\overrightarrow{w}\theta\rangle_s) - \frac{n_s}{m_s}\left\langle \overrightarrow{F_s} \cdot \bigtriangledown_{\overrightarrow{w_s}}\theta \right\rangle_s = \int \theta_s \left[\frac{\partial f_s}{\partial t}\right]_{el} d\overrightarrow{w_s} + \int \theta_s \left[\frac{\partial f_s}{\partial t}\right]_{ch} d\overrightarrow{w_s} \tag{2.2}$$

where $\langle\cdot\rangle$ denotes the average value of a molecular quantity.

Continuity

The n species continuity equations are obtained by taking $\theta = m_s$:

$$\frac{\partial \rho_s}{\partial t} + \bigtriangledown \cdot \left[\rho_s \left(\overrightarrow{u} + \overrightarrow{U_s}\right)\right] = \omega_s \tag{2.3}$$

where ω_s demotes the chemical source term and $\overrightarrow{U_s}$ denotes the diffusive velocity of s-particles. By adding up Eq.2.1.1 over all species, we obtain the overall continuity equation:

$$\frac{\partial \rho}{\partial t} + \bigtriangledown \cdot (\rho \overrightarrow{u}) = 0 \tag{2.4}$$

where the chemical source term vanishes because no mass is generated during chemical reactions.

Momentum

The global momentum equation is obtained by taking $\theta_s = m_s \overrightarrow{w_s}$ and adding up the n distinct momentum equations:

$$\frac{\partial \rho \overrightarrow{u}}{\partial t} + \bigtriangledown \cdot \left(\rho \overrightarrow{u} \overrightarrow{u} = p\hat{I} - \hat{\tau} \right) + \overrightarrow{E}' n_c + \overrightarrow{J_c} \times \overrightarrow{B} \tag{2.5}$$

where $\hat{\tau}$ is the viscous stress tensor.

Energy

The global energy equation is obtained in the same manner by taking $\theta_s = m_s w_s^2/2$:

$$\frac{\partial \rho E}{\partial t} + \bigtriangledown \cdot (\rho \overrightarrow{u} H) + \bigtriangledown \cdot \left(\sum_s \rho_s \overrightarrow{U_s} h_s \right) + \bigtriangledown \cdot \overrightarrow{q} = \bigtriangledown \cdot (\overrightarrow{u} : \hat{\tau}) + \overrightarrow{J} \cdot \overrightarrow{E} \tag{2.6}$$

where the total energy per unit mass is defined as $E = u^2/2 + e$ and the total enthalpy per unit mass is written as $H = u^2/2 + h$.

Electron Energy

The electron energy equation can be obtained by taking $\theta_e = m_e w_e^2/2$. Here a less cumbersome non-conservative form is used:

$$\frac{\partial \rho_e e_{th-e}}{\partial t} + \bigtriangledown \cdot (\rho_e \overrightarrow{u} h_{th-e}) + \bigtriangledown \cdot \left(\rho_e \overrightarrow{U_e} h_{th-e}\right) + \bigtriangledown \cdot \overrightarrow{q_e} = -\rho_e \overrightarrow{U_e} \cdot \frac{d\overrightarrow{u}}{dt} + \hat{\tau_e} : \bigtriangledown \overrightarrow{u} + (\overrightarrow{u} \cdot \bigtriangledown) p_e + \overrightarrow{J_e} \cdot \overrightarrow{E'} + P_{eh}^e + P_{Ch}^e \tag{2.7}$$

where $\overrightarrow{q_e}$ denotes the electron thermal conduction vector and $\hat{\tau_e}$ stands for the electron viscous tensor.

2.1.2 Electromagnetics

Ohm's Law

We express the electric field $\overrightarrow{E}$ as the sum of $\overrightarrow{E_S}$ and $\overrightarrow{E_I}$:

$$\overrightarrow{E} = \overrightarrow{E_S} + \overrightarrow{E_I} \tag{2.8}$$

where $\overrightarrow{E_S} = -\bigtriangledown \phi$ and $\overrightarrow{E_I} = -\frac{\partial \overrightarrow{A}}{\partial t}$.

Neglecting the contribution of the ions, the conduction current is expressed as:

$$\overrightarrow{J_C} = \sum_s n_s \overrightarrow{U_s} q_s \approx n_e \overrightarrow{U_e} q_e = \overrightarrow{J_e}. \tag{2.9}$$

$\overrightarrow{J_C}$ can be further expressed in the form of Ohm's law:

$$\overrightarrow{J_C} = \sigma \left(\overrightarrow{E_S} + \overrightarrow{E_I} + \overrightarrow{u} \times \overrightarrow{B} - \frac{\bigtriangledown p_e}{n_e q_e}\right) \tag{2.10}$$

where $\sigma = \frac{n_e^2 q_e^2}{p_e \sum_{j \neq e} x_j D_{ej}}$.

Helmholtz Induction Equation

The induced electric field $\overrightarrow{E_I}$ inside the torch acts in the toroidal direction and is modeled by using a single Fourier mode

$$\overrightarrow{E_I} = E_I \exp(i2\pi ft)\ \mathbf{e}_\theta \tag{2.11}$$

where f is the torch operating frequency. At the operating conditions of interests, the magnetic Reynolds number is relatively small and the electric field can be computed by using Helmholtz induction equation, as follows:

$$\frac{\partial}{\partial z}E_I + \frac{1}{r}\frac{\partial}{\partial z}\left(r\frac{\partial}{\partial r}E_I\right) - \frac{1}{r^2}E_I - i\mu_0 2\pi f\sigma E_I = i\mu_0 2\pi f J_V \tag{2.12}$$

where μ_0 is the magnetic permeability of free space. To take into account phase differences inside the torch, E_I stands for a complex variable.

The radio-frequency electromagnetic field generates small oscillating perturbations on all flow-field quantities. By averaging the flow equations in time, a quasi-steady flow formulation similar to the steady NavierStokes equations is obtained. In the momentum equation, a time-averaged Lorentz force (F_L) appears, whereas in the energy equation a time-averaged Joule heating source term (P_J) must be taken into account.

2.2 Thermodynamic Properties

A detailed overview of the thermodynamic models can be found in previous works on air plasmas [1, 16, 2, 30]. Quantum physics describes how molecules and atoms store the energy in different modes, each of which is quantized. In the present work, the thermodynamic properties have been computed considering the internal modes of the different species and making the assumption of rigid harmonic oscillator for the diatomic molecules. In such a case, the rotational, vibrational, and electronic energy modes are considered independent from each other and thermodynamic properties

of individual species (and of the mixture) follow from straightforward statistical mechanics considerations [49]. Moreover, only a finite number of electronic levels needs to be taken into account [16] and here we consider the strictly minimum number of electronic levels that produces a non-negligible change of energy in the temperature range of interest in this research. In this section, the resistive MHD equations derived in the preceding section will be extended to a more realistic form considering the internal degrees of freedom.

In this work, the ionized air is represented by a mixture of eleven species:

- Neutral species: N_2, O_2, NO, N, O
- Charged species: N_2^+, O_2^+, NO^+, N^+, O^+, e^-.

The discrete quantum states of the species (discrete electronic quantum states for all particles and discrete rotational and vibrational quantum states for molecular species) should be treated in a coupled manner. However, it has been shown that the coupling effects for the operating conditions considered here have a minimal influence on the computed results (of the order of 1%). Therefore, we treat treat molecular particles based on the rigid rotator and harmonic oscillator assumptions.

2.2.1 Statistical Mechanics

According to statistical mechanics, the excited states of the heavy particles of our two-temperature formulation are populated according to a two-temperature Boltzmann distribution:

$$\frac{n_s^{r,v,e}}{n_s} = \frac{g_{rot,s}^r g_{vib,s}^v g_{el,s}^e exp\left(-\epsilon_{rot,s}^r/k_B T_{hr}\right) exp\left(-\left(\epsilon_{vib,s}^v + \epsilon_{el,s}^e\right)/k_B T_{ev}\right)}{Q_{rot,s} Q_{vib,s} Q_{el,s}} \tag{2.13}$$

where $n_s^{r,v,e}$ is the number density in the (r, v, e) quantum state of s particles and $Q_{rot,s}$, $Q_{vib,s}$ and $Q_{el,s}$ are the partition functions given by:

$$Q_{M,s} = \sum_{m=0}^{\infty} g_{M,s}^m exp\left(-\epsilon_{M,s}^m/k_B T_M\right) \tag{2.14}$$

Rotational Energy

$Q_{rot,s}$ is expressed as:

$$Q_{rot,s} = \frac{T_{hr}}{\sigma_s \theta_{rot,s}} + \frac{1}{3\sigma_s} + \frac{\theta_{rot,s}}{15\sigma_s T_{hr}} \tag{2.15}$$

where $\theta_{rot,s}$ stands for the characteristic temperature of rotational energy and σ_s is the symmetry number. The rotational energy per unit mass of s particles then reads:

$$e_{rot,s} = (k_B/m_s)\, T_{hr} \left(1 - \frac{\theta_{rot,s}}{\theta_{rot,s} + 3T_{rot,s}}\right). \tag{2.16}$$

Vibrational Energy

$Q_{vib,s}$ is written as:

$$Q_{vib,s} = \frac{1}{1 - exp\left(-\sigma_{vib,s}/T_{ev}\right)} \tag{2.17}$$

where $theta_{vib,s}$ is the characteristic temperature of s particles and the vibrational energy per unit mass reads:

$$e_{vib,s} = (k_B/m_s)\, \frac{\theta_{vib,s}}{exp\left(\theta_{vib,s}/T_{ev} - 1\right)}. \tag{2.18}$$

Electronic Energy

The explicit formula for the electronic energy reads:

$$Q_{el,s} = \sum_{e=0}^{\infty} g^e_{el,s} exp\left(-\epsilon^e_{el,s}/k_B T_{ev}\right). \tag{2.19}$$

Truncating the sum by a maximum energy level $e_{max,s}$ the electronic energy per unit mass is expressed as:

$$e_{el,s} = (k_B/m_s)\, \frac{\sum_{e=0}^{e_{max,s}} g^e_{el,s} \epsilon^e_{el,s} exp\left(-\sigma^e_{el,s}/k_B T_{ev}\right)}{k_B Q_{el,s}}. \tag{2.20}$$

2.2.2 Flow Field Governing Equations of the Two-temperature Formulation

The internal degrees of freedom is incorporated into the flow field governing equations by treating the inelastic collisions between different quantum states as chemical reactions.

Continuity

The continuity equation for a specific quantum state of the s species reads:

$$\frac{\partial \rho_s^{r,v,e}}{\partial t} + \bigtriangledown \cdot \left[\rho_s^{r,v,e} \left(\overrightarrow{u} + \overrightarrow{U_s^{r,v,e}} \right) \right] = \omega_s^{r,v,e}. \tag{2.21}$$

The continuity equations for s particles is obtained by adding up the above equations for all quantum states:

$$\frac{\partial \rho_s}{\partial t} + \bigtriangledown \cdot \left[\rho_s \left(\overrightarrow{u} + \overrightarrow{U_s} \right) \right] \tag{2.22}$$

where

$$\overrightarrow{U_s} = (1/\rho_s) \sum_{r,v,e} \rho_s^{r,v,e} \overrightarrow{U_s^{r,v,e}}. \tag{2.23}$$

The global continuity equation then reads:

$$\frac{\partial \rho}{\partial t} + \bigtriangledown \cdot (\rho \overrightarrow{u}) = 0. \tag{2.24}$$

Momentum

The global momentum equation remains unchanged:

$$\frac{\partial \rho \overrightarrow{u}}{\partial t} + \bigtriangledown \cdot \left(\rho \overrightarrow{u} \overrightarrow{u} + p\hat{I} - \hat{\tau} \right) = \frac{1}{\mu_0} \left(\bigtriangledown \times \overrightarrow{B} \right) \times \overrightarrow{B}. \tag{2.25}$$

Internal Energy

The internal energy for mode M (rot, vib, el) is given by $e_M = \sum_s y_s e_{M,s}$ and the corresponding governing equation reads:

$$\frac{\partial \rho e_M}{\partial t} + \bigtriangledown \cdot (\rho \overrightarrow{u} e_M) + \bigtriangledown \cdot \left(\sum_s \rho_s \overrightarrow{U_s} e_{M,s} \right) = \bigtriangledown \cdot (\Lambda_M \bigtriangledown T_M) + \sum_{s,r,v,e} \frac{\epsilon_{M,s}^{r,v,e} \omega_s^{r,v,e}}{m_s} \tag{2.26}$$

where $T_M = T_{hr}$ for M = rot and T_{ev} for M = (vib,el). The mixture's thermal conductivity Λ_M is given by:

$$\Lambda_M = n \sum_s \frac{x_s \hat{C}_{p,I,s}}{\sum_{j \neq e} (x_j / D_{sj})}. \tag{2.27}$$

Total Energy

The total energy equation is obtained by adding up all the rotational, vibrational and electronic energy modes:

$$\frac{\partial \rho e}{\partial t} + \bigtriangledown \cdot (\rho \overrightarrow{u} h) + \bigtriangledown \cdot \left(\sum_s \rho_s \overrightarrow{U_s} h_s \right) = \bigtriangledown \cdot [(\lambda_h + \lambda_r) \bigtriangledown T_{hr}] + \bigtriangledown \cdot [(\lambda_v + \lambda_{el} + \lambda_e) \bigtriangledown T_{ev}] + P_J. \tag{2.28}$$

Electro-vibrational Energy

By adding up the electron translational energy and the molecular particles' vibrational and electronic energies, the electro-vibrational energy equation reads:

$$\frac{\partial \rho e_{ev}}{\partial t} + \bigtriangledown \cdot (\rho \overrightarrow{u} h_{ev}) + \bigtriangledown \cdot \left(\sum_s \rho_s \overrightarrow{U_s} h_{ev,s} \right) + \bigtriangledown \cdot [(\lambda_v + \lambda_{el} + \lambda_e) \bigtriangledown T_{ev}] + (\overrightarrow{u} \cdot \bigtriangledown) p_e + P \tag{2.29}$$

where $P = P_J + P_{El}^e + P_{Inel}^{ev} + P_{Ch}^{ev}$.

2.3 Transport Properties

2.3.1 Heavy Particle Transport Properties

The modified Chapman-Enskog perturbative analysis for partially ionized plasmas [16, 12] is the basis for the computation of transport coefficients and fluxes. Efficient iterative algorithms [31] are used to solve the linear systems for the shear-viscosity and the translational thermal conductivity. This is not only more accurate but also computationally cheaper than using mixture rules such as Yos'[51] as is the case in many high Mach number high enthalpy solvers. The rotational, vibrational and electronic thermal conductivities are modeled by means of the Eucken approximation [16, 12]. The electron thermal conductivity and electrical conductivity are computed using two non-vanishing Laguerre-Sonine polynomial contributions. The obtained expressions are identical to the formulas of Devoto [10], which were found to yield accurate results [16]. The diffusion fluxes have been computed solving the well-known Stefan-Maxwell system of equations [16, 12, 32] which consists of a linear system (in the diffusion fluxes) of as many equations as the chemical species in the mixture, supplemented by the auxiliary condition that the sum of the diffusion fluxes is zero plus the ambipolar constraint. They are perfectly equivalent, by derivation, to the complete diffusion equations, but remarkably less computationally expensive than the latter.

Heavy Particle Transport Fluxes

The $n-1$ heavy particle diffusion velocities are evaluated using the Stefan-Maxwell relations:

$$\sum_{j \neq e} \frac{x_s x_j}{D_{sj}} \left(\overrightarrow{U_j} - \overrightarrow{U_s} \right) - k_{T-s} \bigtriangledown log T_h = \overrightarrow{d_s} \tag{2.30}$$

where D_{sj} stands for the binary diffusion coefficients.

The heavy particle conductive heat fluxes are given by:

$$\overrightarrow{q_h} = \sum_{s \neq e} \overrightarrow{q_s} = -\Lambda \bigtriangledown T_h + n k_B T_h \sum_{s \neq e} k_{T-s} \overrightarrow{U_s} \tag{2.31}$$

where Λ_h denotes the heavy particle thermal conductivity.

Mixture Properties

Hirschfelder Formula

According to the rigorous formulations derived by Hirschfelder, Curtiss and Bird [], the transport properties of gas mixtures can be expressed as ratios of determinants. the first approximations to the viscosity μ^1 and translational thermal conductivity Λ_h^1 read:

$$\mu^1 \text{ or } \Lambda_h^1 = \frac{\begin{vmatrix} A_{1,1} & \cdots & A_{1,n-1} & x_1 \\ \vdots & & \vdots & \vdots \\ \vdots & & \vdots & \vdots \\ A_{n-1,1} & \cdots & A_{n-1,n-1} & x_{n-1} \\ x_1 & \cdots & x_n & 0 \end{vmatrix}}{|A_{s,j}|}. \tag{2.32}$$

Yos Mixture Rule

The computational costs in evaluating the determinants can be very high thus various approximations have been developed by researchers in order to reduce the costs which are known as mixture rules. For neutral gas mixtures, the contribution from the off-diagonal elements is fairly small and a straightforward simplification is obtained by neglecting these elements. This approximation can be problematic for ionized gas mixtures since charged-charged and charged-neutral interactions can be very important. A more accurate expression is proposed by Yos by replacing the off-diagonal elements by an averaged value.

2.3.2 Electron Transport Properties

Electron Transport Fluxes

Again, the electron diffusion velocity obeys the Stefan-Maxwell relation:

$$-\sum_{j\neq e}\frac{x_e x_j}{D_{ej}}\overrightarrow{U_e} \; - \; -k_{T-e}\bigtriangledown logT_e \; = \; \frac{T_h}{T_e}\overrightarrow{d_e} \tag{2.33}$$

and the electron heat conductive flux reads:

$$\overrightarrow{q_e} \; = \; -\Lambda_e \bigtriangledown T_e \; + \; nk_B T_e k_{T-e}\overrightarrow{U_e}. \tag{2.34}$$

Electrical Conductivity and Electron Thermal Conductivity

The electrical conductivity obtained using a single non-vanishing Sonine polynomial reads:

$$\sigma^1 \; = \; \frac{3n_e q_e^2 \left(8k_B T_e/\pi m_e\right)^{-1/2}}{4m_e \sum_{j\neq e} n_j \overline{\Omega}_{ej}^{11}} \tag{2.35}$$

In a similar manner, the electron thermal conductivity is expressed as:

$$\Lambda_e^1 \; = \; (76k_B/64)\,\frac{x_e \left(\pi k_B T_e/m_e\right)^{1/2}}{x_e\overline{\Omega}_{ee}^{22} \; + \; \left(1/\sqrt{2}\right)\sum_{j\neq e} x_j \left[25/4\overline{\Omega}_{ej}^{11} \; - \; 15\overline{\Omega}_{ej}^{12} \; + \; 12\overline{\Omega}_{ej}^{13}\right]}. \tag{2.36}$$

2.3.3 Diffusion in Two-temperature Formulation

The Stefan-Maxwell Equations

Binary Diffusion Coefficients

The formula for the binary diffusion coefficient D_{sj} in the Stefan-Maxwell relation is given by considering a single, non-vanishing Sonine polynomial contribution:

$$D_{sj}^1 \; = \; \frac{3\left(2\pi\mu_{sj}k_B T_{sj}\right)^{1/2}}{16n\mu_{sj}\overline{\Omega}_{sj}^{11}T_{sj}} \tag{2.37}$$

where the reduced mass is given by $\mu_{sj} = m_s m_j / (m_s + m_j)$.

Ramshaw and Chang [] proposed a different formulation:

$$D_{sj}^{1,RC} = \frac{3k_B^2 T_s T_J \left(2\pi\mu_{sj}/k_B T_{sj}\right)^{1/2}}{16 p \mu_{sj} \overline{\Omega}_{sj}^{11} T_{sj}}. \tag{2.38}$$

Formulation of Ramshaw and Chang

The Ramshaw and Chang formulation takes the following form:

$$\sum_j \frac{z_s z_j}{D_{sj}^{1,RC}} \left(\overrightarrow{U_j} - \overrightarrow{U_s}\right) = \bigtriangledown z_s - \frac{n_s q_s}{p} \overrightarrow{E_A} \tag{2.39}$$

where z_s represents the partial pressure ratio and $\overrightarrow{E_A}$ stands for the ambipolar electric field.

2.4 Chemistry and Energy Exchanges

When performing calculations with chemically reacting flows, in addition to the equations expressing the conservation of mass, momentum, and energy, the knowledge of the composition and the population of the internal energy modes is needed to compute the transport and thermodynamic properties of the mixture to close the system of equations. For this purpose, in this section, different physico-chemical models are briefly recalled.

2.4.1 LTE Formulation

When chemistry is sufficiently fast with respect to the characteristic time of the flow, the gas reaches a state of local thermodynamic equilibrium. In these conditions, the description of the flow is considerably simplified since the composition is obtained by solving a system of non-linear algebraic equations [3, 49]. This system of equations yields a solution, which is equivalent to the solution of a species conservation PDEs (CNEQ formulation) in the limit of infinitely fast reactions. In this framework, we adopted a classical LTE formulation with constant fraction of elements [47, 43]. In the constant elemental fraction formulation (LTE-CEF), the mixture composition is computed in

the entire domain as a function of pressure and temperature assuming constant elemental fraction equal to the inlet ones.

2.4.2 CNEQ Formulation

Under chemical non-equilibrium conditions, differential equations describe the advection, diffusion and chemical processes make the species concentrations vary within the flow-field. The mass production terms, present in the species continuity equations, are computed using the law of mass-action and require the knowledge of the rates for all the reactions needed to describe the flow behavior. Values of these rates for high-temperature air are available in literature, but they have a relatively large uncertainty. Hence any non-equilibrium analysis is strongly affected by the trustworthiness of the existing rate data. In the present work four different models for the forward reaction rates coefficient have been analyzed, *i.e.*, the Park [14, 45, 46] and DunnKang [11] models. These models give rates values for the forward reaction rates, and in the present study the backward reaction rates have been retrieved making use of the equilibrium constant, according to the principle of detailed balance [49].

2.4.3 NLTE Formulation

Multi-temperature models are obviously more complex than CNEQ models in the sense that they allow for the thermal non-equilibrium effects to be accounted for. In this case, the population of each internal energy mode for all species follows a Maxwell-Boltzmann distribution at a specific temperature (rotational T_r, vibrational T_v, or electronic temperature T_e). Moreover, for the chemical kinetics model, the macroscopic rate coefficients are assumed to be dependent on an empirical temperature defined in terms of the different temperatures in the flow. Here, we consider three multi-temperature models: the Knab model [17], the Treanor model [33] and the Park model [45].

2T-Treanor model

The model proposed by Treanor and Marrone can be considered as an extension of the work of Hammerling [15]. The main innovation is due to the introduction of a distribution of dissociation probabilities. The dissociation probabilities among the vibrational levels depend on the vibrational quantum number v, such that:

$$P(v) \propto \exp\left[-(D - \epsilon_v)/k_B U\right] \tag{2.40}$$

where k_B is the Boltzmann constant, D is dissociation energy, and ϵ_v is vibrational energy. In above expression, the parameter U has the dimension of a temperature that generally takes values in the range:

$$\frac{\epsilon_{d,s}}{6k_B} \leq U \leq \frac{\epsilon_{d,s}}{3k_B} \tag{2.41}$$

where $\epsilon_{d,s}$ denotes the dissociation energy of the species s. For an infinite value of U, the model becomes equivalent to the model of Hammerling. Treanor's model relies on the Boltzmann distribution to describe the population of the vibrational levels and assumes that, during dissociation processes, such a distribution is negligibly affected by chemistry. In this model, the non-equilibrium factor has the following expression:

$$Z(T, Tv) = \frac{Q(T)Q(T_F)}{Q(Tv)Q(-U)} \tag{2.42}$$

where Q defines the partition function for a truncated harmonic oscillator and T_F is an average temperature defined as follows:

$$T_F = \left(\frac{1}{Tv} - \frac{1}{T} - \frac{1}{U}\right)^{-1} \tag{2.43}$$

Da Silva in [8] compares the dissociation rates obtained with multi-temperature models against those given by a state-to-state approach. According to the study, Treanor's model nicely predicts the dissociation rates for molecule-molecule collisions at high temperatures, as the prediction errors do not exceed one order of magnitude. However, at low temperatures (in the order of a few thousands

degrees), the model tends to over-predict the rate of dissociation. The interaction atom-molecule is predicted rather well by the model within the range of interest for hypersonic applications. In conclusion, Treanor's model provides an acceptable representation of the dissociation rates in compression or expansion flows, even if the fair agreement found in [8] for an expanding flow seems to be coincidental.

2T-Park model

The Park model [45] has been widely accepted as a standard model to account for thermo-chemical non-equilibrium effects. It is based on a geometric average of temperature

$$T_a = T^{1-q_i} T_v^{q_i} \tag{2.44}$$

where q_i is a vibration-dissociation coupling term for the i^{th} reaction. The value of q_i is customarily set to 0.5, based primarily on physical intuition. It will be considered an uncertain parameter in the current study. Furthermore, different values of the parameter will be used for Nitrogen and Oxygen dissociation in order to account for the differences in the dynamics of dissociation for the two molecules. Thus, in the following, q_{N_2} refers to the coupling coefficient for Nitrogen dissociation while q_{O_2} to the coefficient for Oxygen dissociation.

In addition to q_{N_2} and q_{O_2}, we also consider the vibrational energy removal coefficients, C_{N_2} and C_{O_2}, as an uncertain parameters. Many models for vibration-dissociation coupling have been developed over the years . Candler and Nompelis have concluded in [6] that it is sometimes difficult to interpret the experimental data used to derive the constants for the Arrhenius expression of the forward reaction rate, a critical issue that limits the accuracy of these models. In some cases, for instance, the reaction rates were measured in shock-heated gas that was in a state of thermo-chemical non-equilibrium. It is therefore important to interpret the experimental data in a manner that is consistent with the vibration-dissociation model being used. For the current investigation,

the vibrational energy lost through dissociation is given by

$$\Omega^{CV} = \sum_{m \in \mathcal{V}} C_m \left(\sum_{r \in \mathcal{R}^m} \dot{\omega}_{mr} \right) \mathcal{D}^m \tag{2.45}$$

where $\mathcal{R}^m$ is the set of reactions that involve molecule m and $\mathcal{D}^m$ represents the dissociation energy per unit mass of the diatomic molecules involved in the dissociation (or recombination) reaction m. The parameter C_m describes the fraction of dissociation energy removed by the dissociation of the m^{th} molecule. The recommended value for C_m is 0.3, but this value remains quite uncertain, since a value of 0.8 can also be found in the literature [13].

Knab model

Knab *et al* [17] extended Treanor's model to other reactions, adopting the same philosophy used by Treanor and Marrone and assuming that the chemical reactions do not affect the vibrational distribution function. Knab's model, disregarding anharmonicity effects, uses the well known trunked harmonic oscillator model. Thus, indicating with $Q_{V_m}^{\theta_m^D}(T_V)$ the vibrational partition function (trunked oscillator) of molecule m at the temperature T_V, we have:

$$Q_{V_m}^{\theta_m^D}(T_V) = \frac{1 - \exp\left(-\frac{\theta_m^D}{T_V}\right)}{1 - \exp\left(-\frac{\theta_m^V}{T_V}\right)} \tag{2.46}$$

where θ_m^D is the characteristic dissociation temperature and θ_m^V is the characteristic vibrational temperature. For dissociation-recombination reactions the forward reaction rate constant is given by:

$$k_f = Z(T, T_V)\, C T^{\eta} e^{-\theta_m^D / T} \tag{2.47}$$

where:

$$Z(T, T_V) = \frac{Q_{V_m}^{\theta_m^D}(T)}{Q_{V_m}^{\theta_m^D}(T_{vm})} \left[\frac{e^{-\alpha\theta_m^D/T} Q_{V_m}^{\alpha\theta_m^D}(\Gamma_m) + Q_{V_m}^{\theta_m^D}(T_m^0) - Q_{V_m}^{\alpha\theta_m^D}(T_m^0)}{e^{-\alpha\theta_m^D/T} Q_{V_m}^{\alpha\theta_m^D}(-U) + Q_{V_m}^{\theta_m^D}(T^*) - Q_{V_m}^{\alpha\theta_m^D}(T^*)} \right] \tag{2.48}$$

and

$$\begin{cases} \Gamma_m = \left(\dfrac{1}{T_{vm}} - \dfrac{1}{T} - \dfrac{1}{U}\right)^{-1} \\ \\ T^* = \left(\dfrac{1}{T} - \dfrac{1}{U}\right)^{-1} \\ \\ T_m^0 = \left(\dfrac{1}{T_{vm}} - \dfrac{1}{U}\right)^{-1} \end{cases} \tag{2.49}$$

Usually U and α are set equal to $\theta_m^D/3$ and 0.7, respectively.

The influence of the internal excitation on the chemistry, usually limited to the introduction of a correction factor for the dissociation, is extended by Knab *et al* to exchange, associative ionization and electron impact dissociation reactions.

For *exchange reactions* the formulation is similar to dissociation. The rate constant is given by:

$$k_f = Z_3 C T^\eta e^{-\theta_a/T} \tag{2.50}$$

where θ_a is the activation energy in K:

$$Z_3 = \frac{Q_{V_m}^{\theta_m^D}(T)}{Q_{V_m}^{\theta_m^D}(T_{vm})} \left[\frac{e^{-\alpha\theta_a/T} Q_{V_m}^{\alpha\theta_a}(\Gamma_m) + Q_{V_m}^{\theta_m^D}(T_m^0) - Q_{V_m}^{\alpha\theta_a}(T_m^0)}{e^{-\alpha\theta_a/T} Q_{V_m}^{\alpha\theta_a}(-U) + Q_{V_m}^{\theta_a}(T^*) - Q_{V_m}^{\alpha\theta_m^D}(T^*)} \right] \tag{2.51}$$

The definition of the "temperatures" T^* and T_m^0 is the same as before. In this case m indicates the molecule being destroyed. The expression for the backward rate constant is slightly different from the previous case, taking into account the non-equilibrium effects, as follows:

$$k_b = Z_5 \frac{k_{f_{eq}}}{K_c(T)} = Z_5 \frac{C T^\eta e^{-\theta_a/T}}{K_c(T)} \tag{2.52}$$

where:

$$Z_5 = \frac{Q_{V_m}^{\theta_m^D}(T)}{Q_{V_m}^{\theta_m^D}(T_{vm})} \left[\frac{Q_{V_m}^{\theta_m^D}(T_m^0)}{Q_{V_m}^{\theta_a}(T^*)} \right] \tag{2.53}$$

In Equation 2.53 m refers now to the molecule being created.

For *electron impact dissociation* reactions the equations to be used are the same given for dissociation from heavy particle impact. The only difference is that the free electron temperature T_e replaces T in all expressions.

For *associative ionization* reactions the backward rate constant reads:

$$k_f = CT^{\eta} e^{-\theta_a/T} \tag{2.54}$$

while for the backward rate we have:

$$k_b = Z_5 \frac{CT^{\eta} e^{-\theta_a/T_e}}{K_c(T_e)} \tag{2.55}$$

Finally for *electron impact ionization*:

$$k_f = CT_e^{\eta} e^{-\theta_a/T_e} \text{ and } k_b = \frac{CT_e^{\eta} e^{-\theta_a/T_e}}{K_c(T_e)} \tag{2.56}$$

When Knab's model is not employed, the expression used for forward and backward rate constants, with emphasis on the temperature dependence can be found in Table 2.1.

2.4.4 Vibration-Chemistry-Vibration coupling

The chemical reactions depleting or producing molecules affect the average vibrational energy in the gas. Hence the presence of chemistry in the flow imposes the introduction of an additional energy source term into the vibrational energy equations.

Reaction	k_f^r	k_b^r
Exchange	$k_f = CT^\eta e^{-\theta_a/T}$	$k_b = \dfrac{CT^\eta e^{-\theta_a/T}}{K_c(T)}$
Associative ionization	$k_f = CT^\eta e^{-\theta_a/T}$	$k_b = \dfrac{CT_e^\eta e^{-\theta_a/T_e}}{K_c(T_e)}$
Electron impact ionization	$k_f = CT_e^\eta e^{-\theta_a/T_e}$	$k_b = \dfrac{CT_e^\eta e^{-\theta_a/T_e}}{K_c(T_e)}$

Table 2.1: Recommendation for multiple temperature rate constants for different types of reactions.

The source term Ω_m^{CV} is given by the following expression:

$$\Omega_m^{CV} = G_{app_{rm}}\,\dot{\omega}_m^f + G_{va_{rm}}\,\dot{\omega}_m^b \tag{2.57}$$

where $G_{app_{rm}}$ indicates the average vibrational energy lost due to chemistry and $G_{va_{rm}}$ represents the average vibrational energy gained thanks to chemistry. The terms $\dot{\omega}_m^f$ and $\dot{\omega}_m^b$ are the terms of destruction and production of the molecule m due to chemistry.

The determination of the exact amount of energy depleted by a specific chemical reaction is a challenging task, which can be accomplished rigorously in the framework of a state-to-state (or collisional radiative models) approach [41, 42, 39, 40, 38, 37]. However the applicability of such approaches to CFD is restricted due to the large number of equations to be solved and to the huge number of kinetic processes to be modeled.

In literature different models have been created to correctly account for the vibrational energy losses due to dissociation reactions. Among them it is common to distinguish between *preferential* and *non-preferential* dissociation models. The non-preferential models prescribe an equal probability of dissociation from all the quantum levels of the molecules as opposed to the preferential dissociation model based on the assumption that dissociation takes place from the upper vibrationally excited states. Hence the molecules in the lower vibrationally excited states must *ladder climb* to the higher states before dissociating.

The most commonly used models based on the preferential-dissociation concept in the literature are now briefly outlined, highlighting the hypotheses on which each of them rely.

Treanor and Marrone

The main hypotheses of this model were outlined in Section 2.4.4, when discussing the effects of the vibration on chemistry. This leads to the following expression for the the mean energy lost ($G_{app_{rm}}$) or gained ($G_{va_{rm}}$)

$$\begin{cases} G_{app_{rm}} = \frac{R_i \theta_m^v}{e^{-\theta_m^v/U}-1} - \frac{R_i \theta_m^D}{e^{-\theta_m^D/U}-1} \\ \\ G_{va_{rm}} = \frac{R_i \theta_m^v}{e^{\theta_m^v/T_F}-1} - \frac{R_i \theta_m^D}{e^{\theta_m^D/T_F}-1} \end{cases} \tag{2.58}$$

where θ_m is the dissociation energy in K and the averaged temperature has the following expression:

$$T_F = \left(\frac{1}{T_V} - \frac{1}{T} - \frac{1}{U} \right)^{-1} \tag{2.59}$$

Since U characterize the distribution of the dissociation probabilities the energy loss or gained is strongly affected by its definition. Experimentally was observed that behind a shock wave the energy lost due to dissociation corresponds to about 30 % of the dissociation energy.

Knab's model [17] is a preferential dissociation model which extends the work of Treanor and Marrone to exchange and associative ionization reaction. The expressions for the energy exchange source term can be found in Ref.[17].

Non-preferential models

As the free-stream kinetic energy becomes much larger than the dissociation energy of the

molecules, dissociation tends to occur with equal probability from all the levels and the ladder climbing process is not required to dissociate. The simplest of the models which does not account for the preferential dissociation is due to Candler [7] and the energy loss is given by ($\Omega_m^{CV} = c_1\, e_m^V \dot{\omega}$). The constant introduced (c_1) is equal to one for non-preferential models and it assumes values larger than one when preferential dissociation is accounted for.

Chapter 3

Numerical Method

In our numerical model, both the electromagnetic and flow field equations are discretized by means of a second-order accurate finite volume method implemented within COOLFluiD [24, 26, 23, 18, 25], an open computational platform for multi-physics and plasma [9, 50, 40, 36] in particular. The COOLFluiD ICP solver relies upon the AUSM+up scheme [27] for discretizing convective fluxes and upon a central treatment of diffusive fluxes.

The discretized equations are solved using an incomplete Newton method, where flow and electromagnetics are weakly coupled through the RHS but feed two separate linear systems. A GMRES algorithm combined with the Additive Schwartz preconditioning method is used to solve those two systems in parallel simulations.

All results to be shown have been computed on a structured mesh of 200 by 100 cells, which has proved to be fine enough to provide grid converged solutions for this case. Those results are at least six orders of magnitude converged (based on the drop in the L2 residual norm of roto-translational temperature).

3.1 Advection Upwind Splitting Method (AUSM)

The Advection Upwind Splitting Method was devised by M. S. Liou et al. [29, 28] in the early ninety's. This scheme defines a suitable interface advection Mach number in order to calculate the convective properties in an upwind manner and is renowned for combining the robustness of the Roe scheme and the relative simplicity of the Van Leer scheme. In this section, we intend to present a brief introduction to the AUSM family of flux splitting schemes.

3.1.1 The Basic AUSM scheme

Consider a 1D inviscid equations of a generaly Euler conservation law:

$$Q_t + F(Q)_x = 0 \tag{3.1}$$

and discretize using the Finite Volume Method:

$$Q_j^{n+1} = Q_j^n + \frac{\triangle t^n}{\triangle x_j}\left[F_{j+1/2} - F_{j-1/2}\right] = 0 \tag{3.2}$$

where $Q = \begin{bmatrix} \rho \\ \rho u \\ \rho E \end{bmatrix}$ and $F = \begin{bmatrix} \rho u \\ \rho u^2 + p \\ \rho u H \end{bmatrix}$.

The essence of the AUSM schemes is to split the convective flux F^C and a pressure flux P such that:

$$F = F^C + P \; with \, F^C = u \begin{bmatrix} \rho \\ \rho u \\ \rho H \end{bmatrix} = M \begin{bmatrix} \rho a \\ \rho u a \\ \rho H a \end{bmatrix}, \; P = \begin{bmatrix} 0 \\ p \\ 0 \end{bmatrix}. \tag{3.3}$$

The above equation can further be discretized as:

$$F_{1/2} = M_{1/2} \begin{bmatrix} \rho a \\ \rho u a \\ \rho H a \end{bmatrix}_{L/R} + P_{1/2} \; with \; (\bullet)_{L/R} = \begin{cases} (\bullet)_L & M_{1/2} \geq 0 \\ (\bullet)_R & M_{1/2} < 0 \end{cases} \tag{3.4}$$

or in an alternative form:

$$F_{1/2} = M_{1/2}\frac{(\Phi_L + \Phi_R)}{2} - \left|M_{1/2}\right|\frac{(\Phi_R - \Phi_L)}{2} + P_{1/2} \; with \Phi_{L/R} = \begin{bmatrix} \rho a \\ \rho u a \\ \rho H a \end{bmatrix} \tag{3.5}$$

where $M_{1/2}$ is obtained by combining the left and the right states of the interface: $M_{1/2} = M_L^+ +$

M_R^- where M_L and M_R are functions of the Mach number at the left and right states of the interface: The AUSM scheme borrows from the Van Leer splitting to define the split Mach numbers $M^{+/-}$:

$$M^{\pm} = \begin{cases} \pm 1/2\,(M \pm 1)^2 & |M| \leq 1 \\ 1/2\,(M \pm |M|) & |M| > 1 \end{cases}. \tag{3.6}$$

A polynomial expansion of the characteristic speeds is used to define the pressure term $P_{1/2}$:

$$P^{\pm} = \begin{cases} \frac{p}{4}\,(M \pm 1)^2\,(2 \mp M) & |M| \leq 1 \\ \frac{p}{2}\frac{(M \pm |M|)}{M} & |M| > 1 \end{cases}. \tag{3.7}$$

As is noted from the above formulation, the numerical flux is built as a combination of a Mach number weighted averaged term of the right and left states contributions, a numerical dissipation term as well as the pressure term. The lower the Mach number is, the more centralized the scheme is and as the Mach number marches toward unity, the more upstream the scheme is.

3.1.2 AUSM+up

The AUSM+up scheme added a pressure diffusion term M_p to improve calculations at low Mach numbers, which reads:

$$M_p = -K_p max\left(1 = \sigma\overline{M}^2, 0\right)\frac{p_R - p_L}{\rho_{1/2}a_{1/2}^2}\, with\, \rho_{1/2} = \frac{\rho_L + \rho_R}{2} \tag{3.8}$$

and $\overline{M}^2$ is defined as:

$$\overline{M}^2 = \frac{M_L^2 + M_R^2}{2}\, with\, K_p = 0.25\, and\, \sigma \in [\sigma^*, 1]\; with\, \sigma^* = \frac{2}{1 + \left(M_L\frac{a_L}{a_L^*}\right)^4}. \tag{3.9}$$

A velocity diffusion term is as well added to the pressure flux, which reads:

$$p_u = -K_u P^+ P^-\,(\rho_L + \rho_R)\,a_{1/2}\,(u_R - u_L)\; with\, K_u \approx 0.75. \tag{3.10}$$

3.1.3 AUSM+up for All Speeds

Scaling the pressure diffusion M_p term defined above by a factor f_a dependent on the local Mach number, the AUSM+up for All Speeds scheme is obtained. This scheme tacked the problems caused by small pressure perturbations when the flow stalls. f_a reads:

$$f_a = M_0 (2 - M_0) \, and \, M_0^2 = min\left(1, max\left(\overline{M}^2, M_\infty^2\right)\right). \tag{3.11}$$

The interface speed of sound is also modified:

$$a_{1/2} = min\left(\tilde{a}_L, \tilde{a}_R\right) with \begin{cases} \tilde{a}_L = \frac{a^{*2}}{max(a^*, u_L)} \\ \tilde{a}_R = \frac{a^{*2}}{max(a^*, -u_R)} \end{cases}. \tag{3.12}$$

3.2 Torch Configuration and Operating Conditions

The numerical model for the description of the electromagnetic discharge, presented hereafter, is based on the work of Vanden Abelee,[48]. The torch geometry used in the present simulations is shown in Fig. (3.1). The torch is modeled as a fully axisymmetric configuration in which the (solenoidal) inductor is approximated by a series of nc parallel, current-carrying rings. For simplicity, we assume the rings to be infinitely thin current loops, located at the innermost part of the true coil rings, where most of the electric current is known to run.

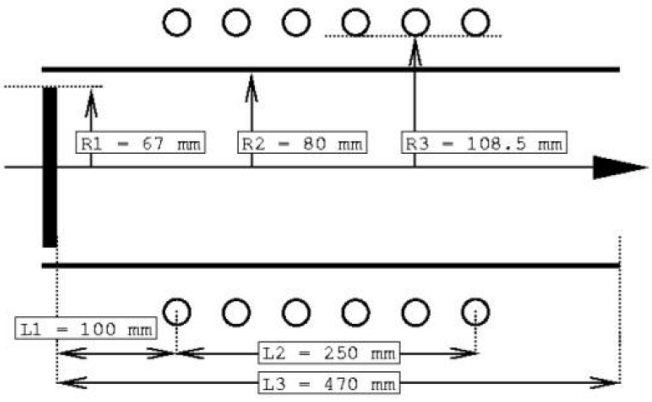

Figure 3.1: Geometry of the VKI plasmatron.

The operating conditions used for the simulations are listed in Tab. (3.1) below.

Ambient and wall temperature, K	300
Power injected into the plasma, kW	$50, 80$
Frequency, MHz	$0.37, 0.45$
Mass flow, g/s	$6, 8$
Operating pressure, Pa	$3000, 5000, 7000, 10000, 15000$

Table 3.1: Plasmatron operating conditions.

Chapter 4

Results and Discussions

In this chapter, numerical results obtained using 1) local thermal-chemical equilibrium formulation (LTE), 2) thermal-chemical non-equilibrium formulation (TCNEQ) are presented and analyzed. Computed contour plots will be compared for qualitative analysis. In order to perform a quantitative analysis, we will also present plots of radial profiles of plasma quantities at either the mid-coil position ($z = 0.265\,m$), or the outlet ($z = 0.470\,m$).

4.1 Thermal-chemical Non-equilibrium Analysis

In this section, simulations are performed with the following operating conditions: outlet pressure $P_o = 3000\,Pa$, mass flow rate $Q = 6\,g/s$, frequency $f = 0.45\,MHz$ and $50\,kW$ for the input power. Park two-temperature chemical-thermo model [45] is implemented to account for thermal non-equilibrium and Park 2001 [46] chemical kinetic model for chemical non-equilibrium.

Figures 4.1a and 4.1b compare the two dimensional distributions obtained by TCNEQ (top) and LTE (bottom) formulations of T_{hr} and T_{ev}, respectively. The LTE formulation predicts a peak temperature above $10000\,K$ on the axis while the TCNEQ formulation presents a substantially lower T_{hr} peak around $6000\,K$ and a larger high temperature zone of T_{hr} on the axis. In agreement with the 2D distribution of X_e (Figure 4.2b), the peak of electron temperature T_{ev} is shifted toward the torch wall where most of electric energy is consumed and dissipated into the plasma through interactions between the electric field and free electrons (Joule heating) and where elastic collisions are insufficient to equilibrate the thermal energies of free electrons and heavy particles.

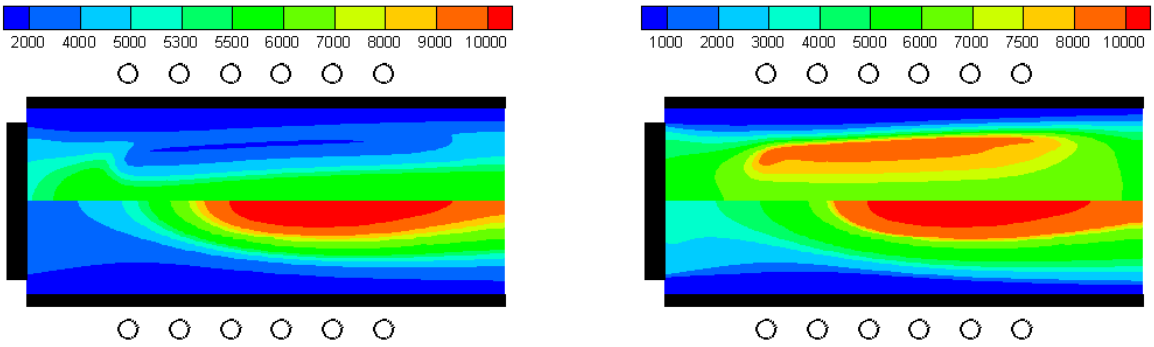

(a) T_{hr} (NEQ, top) vs. T (LTE, bottom)

(b) T_{ev} (NEQ, top) vs. T (LTE, bottom)

Figure 4.1: Comparison of NEQ and LTE models: temperature contours.

Consequently, T_{ev} predicted by TCNEQ formulation is apparently higher than T_{hr} especially near the torch wall where high gradients unfavorable for thermal equilibrium are found. To illustrate the degree of thermal non-equilibrium, T_{ev}/T_{hr}, the ratio of free electron to heavy particle temperatures is introduced by Morsli et al. and is adopted here (Figure 4.2a).

Radial temperature distributions by the LTE and TCNEQ formulations are illustrated in Figures 4.7a and 4.7b corresponding to the mid-coil location ($z = 0.265\,m$) where the highest Joule heating is found, and the outlet ($z = 0.47\,m$), respectively. In the mid-coil location, significant thermal non-equilibrium is observed and thermal-equilibrium is restricted to a narrow region near the torch wall ($r > 0.066\,m$). T_{ev}/T_{hr} reaches the peak at $r = 0.05\,m$ where the free electron concentration finds its maxima. The temperature difference can be explained by the inefficient elastic collisions between free electrons and heavy particles, compared with diffusive processes as well as other energy transfer mechanisms. At the outlet, the thermal non-equilibrium effect is obviously weaker than at the middle and thermal equilibrium is sustained for $r > 0.06\,m$. The temperature profiles illustrated in Figure 4.7b indicates that, for the operational conditions considered, the plasma is rapidly equilibrated as it leaves the torch and passes the outlet. However, a comparison of the LTE and TCNEQ calculations shows that, even though the plasma somehow reaches thermal equilibrium at the outlet, the thermal equilibrium state found by the LTE model differs strongly

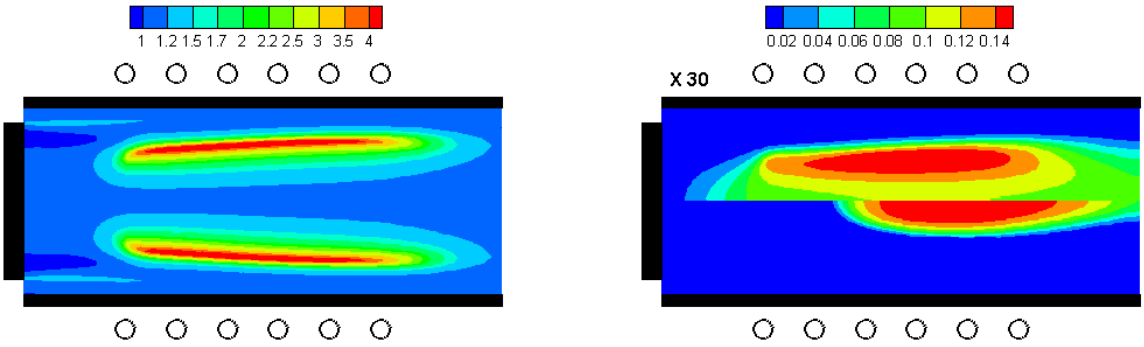

(a) T_{ev}/T_{hr} (b) X_e (NEQ, top) vs. X_e (LTE, bottom)

Figure 4.2: Comparison of NEQ and LTE models: T_{ev}/T_{hr} and X_e contours.

from that found by the TCNEQ formulation. We therefore conclude that the LTE model does not provide an accurate prediction of the plasma properties at the outlet under those operational conditions.

When comparing 2D electric field distributions obtained by TCNEQ (top) and LTE (bottom) formulations in Figure 4.3a, it is found that the electric field is weaker for the TCNEQ formulation. In the TCNEQ calculation, electrons fill a large conducting ring inside the inductor as is illustrated in Figure 4.2b while in the LTE calculation electrons are confined to a narrow zone along the axis. Since more conducting material is present in the TCNEQ calculation, a smaller electric field suffices to reach the prescribed power of $50\,kW$.

4.2 Effects of Chemical Kinetic Models

Accurate description of a reacting mixture requires trustworthy data on the types and rates of chemical reactions present in the mixture. However, the chemistry of ionized air contains many chemical processes whose rate coefficients are inadequately characterized. In particular, the chemistry models currently available for air are well-known for their inaccuracy. Therefore, the chemical kinetic models implemented in the modeling are a source of substantial uncertainty. For instance,

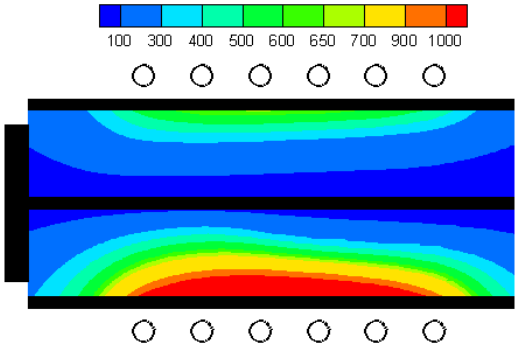

(a) *ElectricalField* (NEQ, top) vs. *ElectricalField* (LTE, bottom)

Figure 4.3: Comparison of NEQ and LTE models: electrical field contour.

a number of reactions included in Park's model [45] do not appear in the model proposed by Dunn and Kang [11] and moreover, for those reactions present in both models reaction rate coefficients may differ by several orders of magnitude. In this section we investigate the dependence of the calculations on the selection of reaction models (Park 89 [44], Park 93 [45], Park 01 [46] and Dunn and Kang [11]) by comparing temperature and species mole fraction distributions obtained by different models.

Figures 4.4a, 4.4b and 4.4c illustrate the radial profile at mid-coil location ($z = 0.265\,m$) of T_{hr}, T_{ev} and T_{hr}/T_{ev}, respectively. As can be seen from these figures, all the four chemical kinetic models predict significant thermal non-equilibrium effects near the torch wall especially the more recent models (Park 93 [45], Park 01 [46]), which, to be noted, present a trough in the radial T_{hr} distribution (Figure 4.4a) where T_{ev} reaches its peak. The deviation from thermal equilibrium near the torch wall is mainly due to high gradients and resulting diffusion effects, however, the reason of the formation of the trough in the radial T_{hr} distribution is still unknown and requires further investigation. Figure 4.6 presents the radial distributions of mole fraction of species e, N^+, O^+, N and O at the mid-coil location obtained using the four chemical kinetic models. LTE predicts a higher electron mole fraction X_e near the axis ($r < 0.034\,m$) but a lower X_e near the torch wall because the diffusion effect is not correctly taken into account. N^+ and

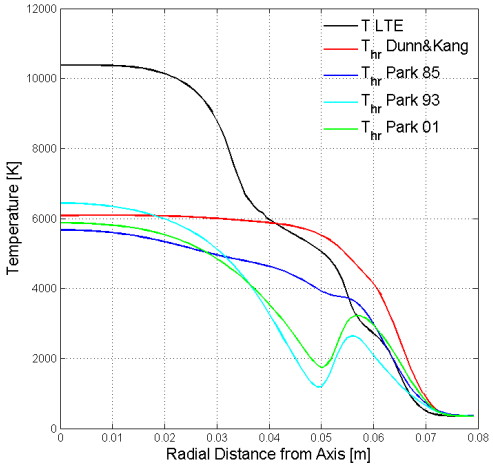

(a) T_{hr}

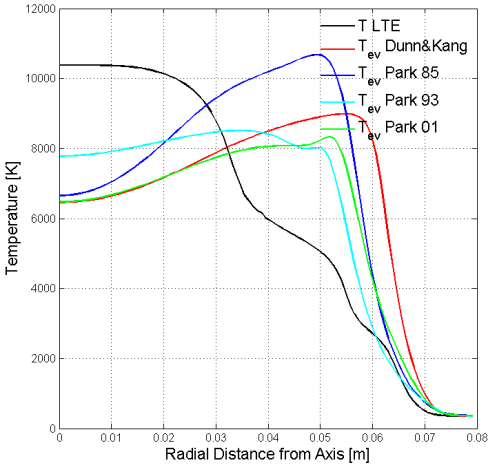

(b) T_{ev}

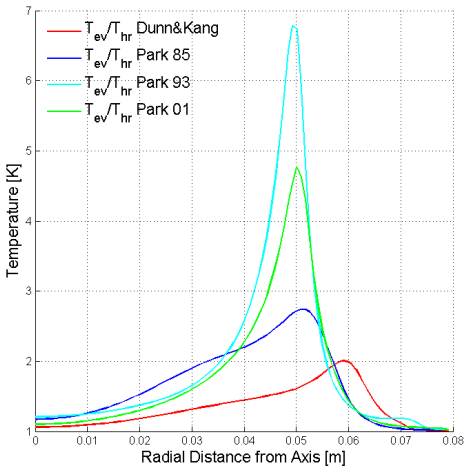

(c) T_{ev}/T_{hr}

Figure 4.4: Temperature profiles at midcoil ($z = 0.265\,m$) by different chemical kinetic models.

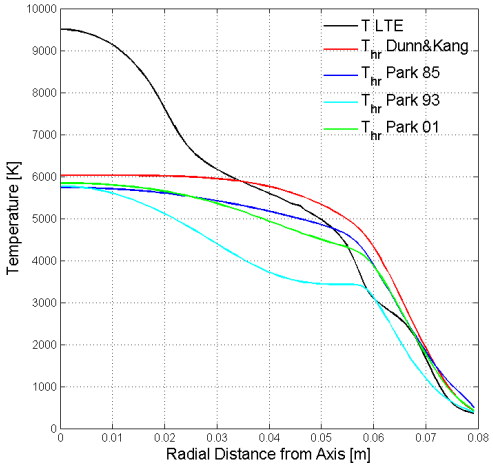

(a) T_{hr}

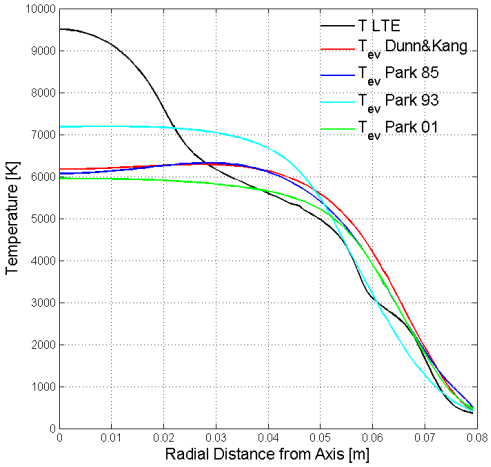

(b) T_{ev}

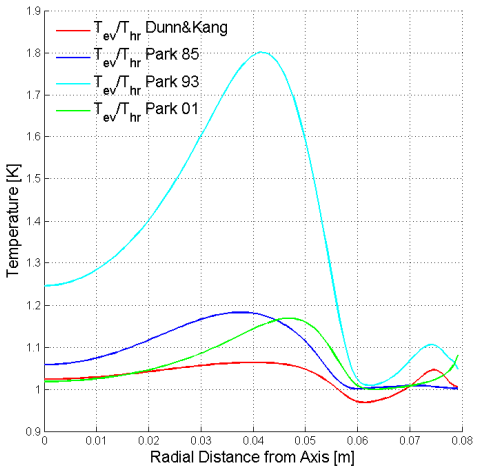

(c) T_{ev}/T_{hr}

Figure 4.5: Temperature profiles at outlet ($z = 0.470\,m$) by different chemical kinetic models.

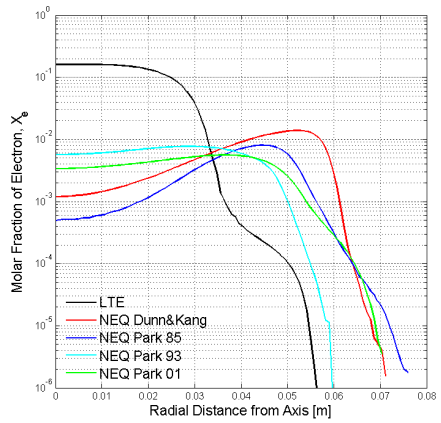

(a) X_e

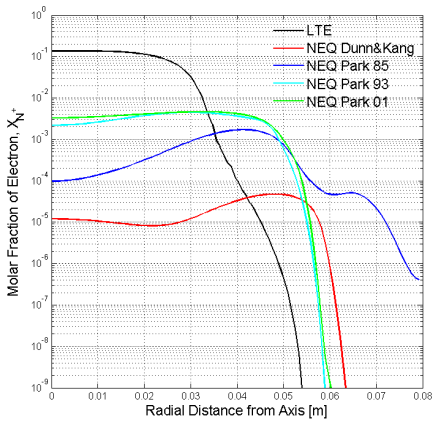

(b) X_{N+}

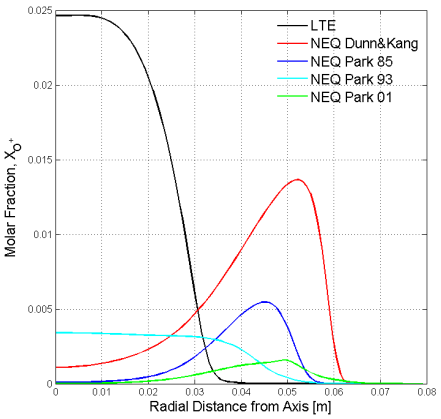

(c) X_{O+}

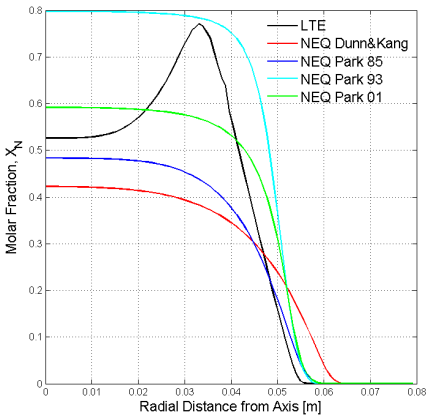

(d) X_N

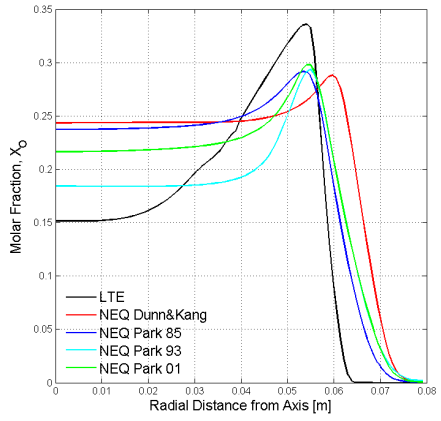

(e) X_O

Figure 4.6: Radial profile of molar fractions of e, N^+, O^+, N and O, predicted by LTE and NEQ models with different chemical kinetic models at mid-coil location ($z = 0.265\,m$).

O^+ demonstrate the same behavior due to finite ionization rates near the axis. The highest atomic nitrogen mole fraction is found to be at $r = 0.034\,m$ with LTE but at the axis with TCNEQ, which is primarily due to significant convective effect near the axis. The deviation from chemical equilibrium is also obvious for atomic oxygen. As illustrated in Figure 4.6, results obtained by different chemical kinetic models in terms of species mole fractions differ from each other up to two orders in magnitude, which indicates a strong dependence of the thermal-chemical non-equilibrium effect on the chemical kinetic model selected. However, considering the tremendous difference between these chemical kinetic models in terms of species, reactions and phenomena involved, we find it extraordinarily difficult to extract intuitive understanding of the relative significant of specific reaction or reaction type among the great number of chemical processes being considered. Thus it is necessary to prioritize the reactions in some manner before further theoretical and experimental investigations. As a first attempt toward such prioritization in ICP modeling, the sensitivity analysis of the chemical mechanisms is conducted in a straightforward way by increasing and decreasing by a factor a 100 the rate coefficients of the five primary reactions of Park 01 model [46]: dissociation, associative ionization, electron-impact ionization, NO exchange and charge exchange. Figure 4.8a and 4.8b show the radial distributions of T_{hr} and T_{ev} respectively at the mid-coil location ($z = 0.265\,m$) obtained by factor of 10 changes in opposite directions. At both locations, it is shown that varying the associative ionization and NO exchange rate coefficients has little impact on the calculated results. Increasing the rate coefficient of charge exchange reactions leads to slightly higher T_{ev} and T_{hr} predictions near the torch axis. It is found that increasing the dissociation rate coefficient increases thermal non-equilibrium by decreasing T_{hr} near the T_{ev} peak while increased electron-impact ionization rate coefficient shows little impact on the temperature distributions at the mid-coil location. The most noticeable influences on the temperature distributions are found for decreased dissociation and electron-impact ionization rate coefficients. By decreasing the electron-impact ionization rate the high temperature region of both T_{hr} and T_{ev} is squeezed toward the axis where a substantial increase in both temperatures is observed. Meanwhile, the high temperature region predicted by simulation with decreased dissociation rate coefficient is not only enhanced but broadened.

Figure 4.9 presents the radial distributions of mole fraction of species e, N^+, O^+, N, O and NO at the mid-coil location. Associative ionization is found to have no impact on the composition of the ionized air mixture at this axial location. The influence of NO exchange reactions on the composition is relatively small except for NO. It is worth noting that factor of 10 change in either direction leads to a substantial increase in the NO concentration especially at the radial location $r = 0.06\,m$. Atomic oxygen O is the least influenced species as is illustrated in Figure 4.9e while atomic nitrogen N demonstrates considerable dependence on dissociation, electron-impact ionization and charge exchange (see Figure 4.9d). Decreased dissociation and electron-impact ionization rate coefficients tremendously increase the ionization of the plasma as is presented in Figure 4.9a - 4.9c.

Park in his 1993 paper [45] found the charge-exchange reactions had little impact on the results of shock tube simulations by varying the rate coefficients and thus arbitrarily removed the reaction $N^+ + N_2 = N + N_2^+$ in his 2001 paper [46]. In this work, however, we find that the role of charge exchange reactions is not that negligible. Simulation with increased charge exchange rate coefficients predicts higher e, N^+ and N concentrations while the generation of O^+ is suppressed. Figure 4.5 presents the radial profile at outlet ($z = 0.47\,m$) of T_{hr}, T_{ev} and T_{ev}/T_{hr}, respectively. From these figures it is observed that at the outlet, although the thermal equilibrium state differs significantly from that obtained using the LTE formulation, thermal equilibrium is indeed reached regardless of the chemical kinetic model implemented, except the Park 93 model, the results of which deviate substantially from thermal equilibrium. The discrepancy between Park 93 and Park 01 models is suspicious since the only modifications made to Park 01 model are the addition of NO exchange and the removal of $N^+ + N_2 = N + N_2^+$ reaction. To elucidate the relative significance of the two reactions, we artificially removed $N^+ + N_2 = N + N_2^+$ and added NO exchange from Park 93 model separately and found that $N^+ + N_2 = N + N_2^+$ was responsible for the discrepancy at the outlet ($z = 0.47\,m$), which reinforced our founding that the role of charge exchange reactions was not negligible in the preceding discussion (see Figure 4.10).

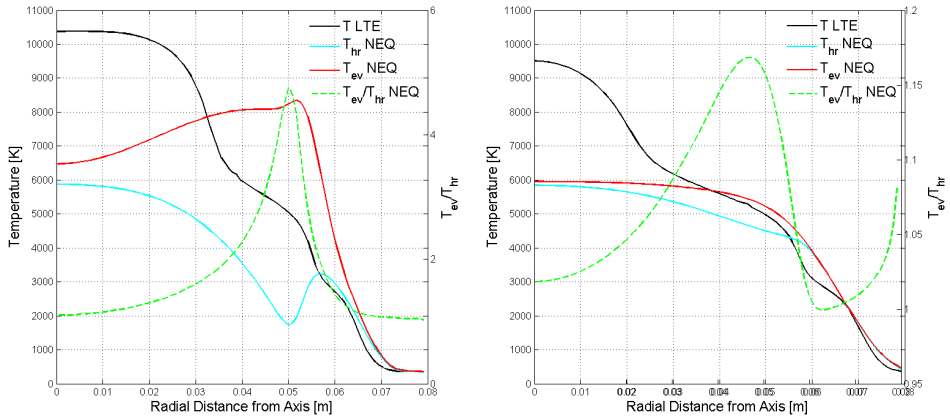

(a) Midcoil ($z = 0.265\,m$) (b) Outlet ($z = 0.470\,m$)

Figure 4.7: Temperature profiles at midcoil and outlet.

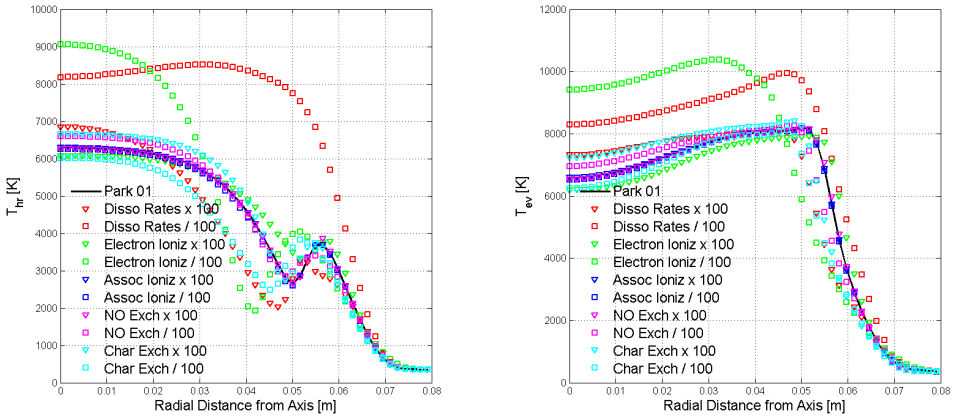

(a) T_{hr} (b) T_{ev}

Figure 4.8: Temperature profiles at mid-coil ($z = 0.265\,m$) showing the impact of various rate coefficients.

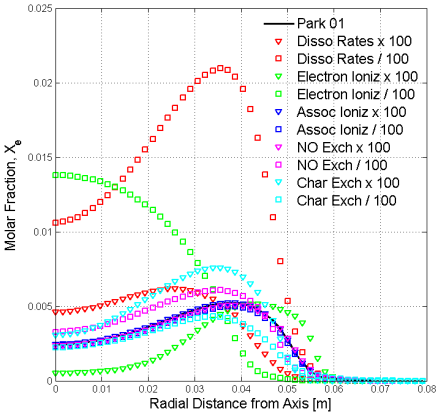

(a) X_e

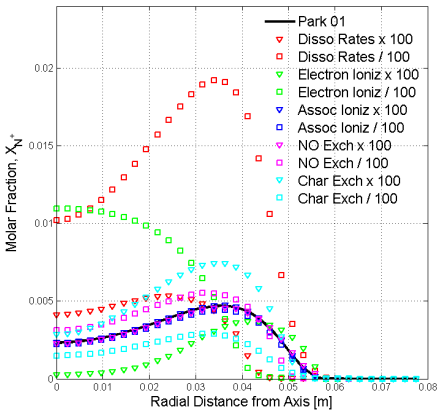

(b) X_{N+}

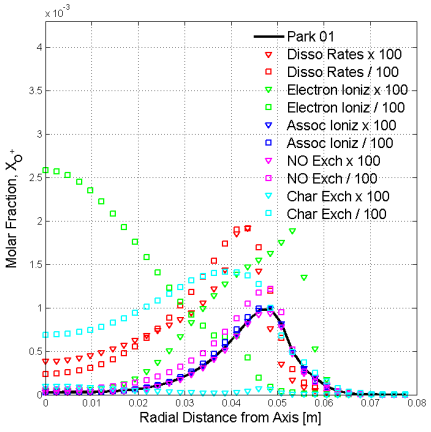

(c) X_{O+}

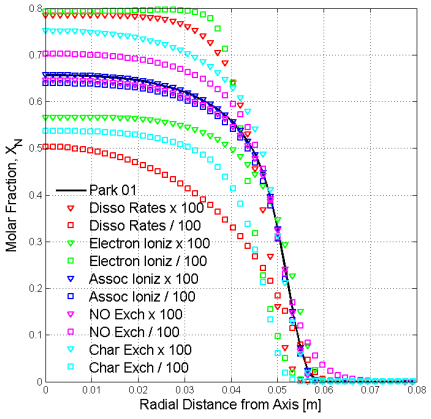

(d) X_N

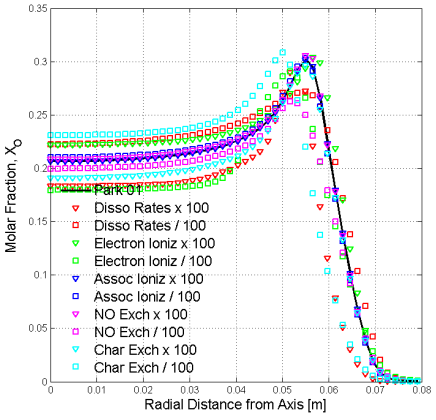

(e) X_O

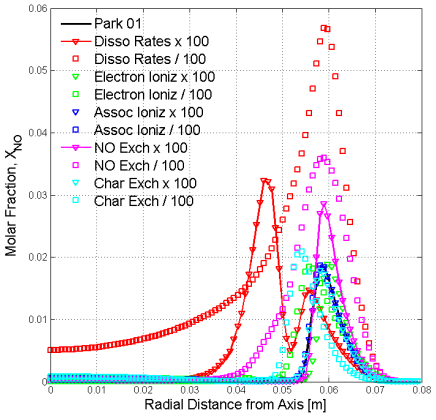

(f) X_{NO}

Figure 4.9: Radial profile of molar fractions of e, N^+, O^+, N, O, NO at mid-coil ($z = 0.265\,m$) showing the impact of various rate coefficients.

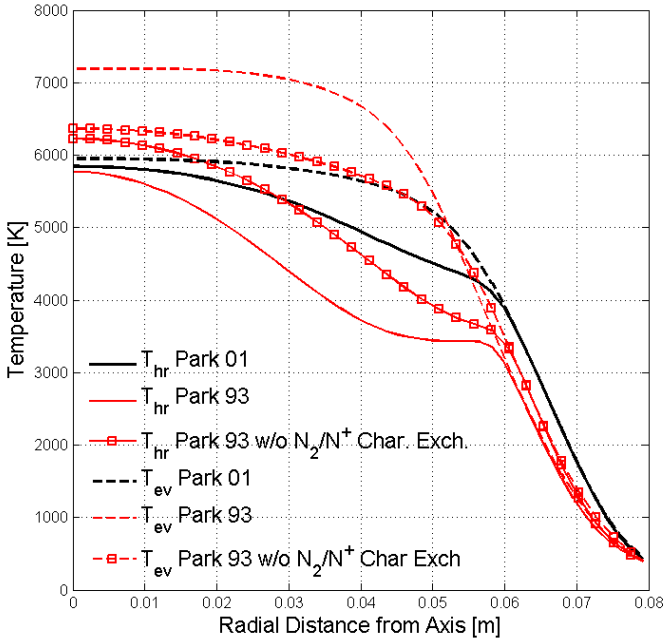

Figure 4.10: Radial profile of temperatures at outlet ($z = 0.47\,m$) showing the impact of $N^+ + N_2 = N + N_2^+$.

4.3 Effects of Multi-temperature Approaches

In this section we discuss the coupling of thermal non-equilibrium and chemistry in the framework of multi-temperature approaches. We here particularly focus on the influence of the non-preferential (Park 2T [45]) and preferential (Treanor [33]) vibration-chemistry coupling models on N_2, O_2 dissociation reactions. Comparisons of these two models are further extended to exchange and ionization reactions through the inclusion of Knab model [17]. Figure 4.11 illustrates the radial distributions of temperatures and electron mole fraction at the mid-coil location ($z = 0.265\,m$) corresponding to the highest Joule heating area obtained by preferential and non-preferential coupling models. The discrepancy between Park coupling model and Treanor coupling model [33] is almost negligible which indicates that under the current operating conditions dissociation reactions are insensitive to the selection of vibration-chemistry coupling models and the simplified non-preferential model assuming that all vibrational levels dissociate with equal probability is sufficient to account for the vibration-dissociation coupling effect. Discernible difference is observed between Knab [17] and Treanor [33] (or Park [45]) coupling models. Knab coupling model predicts higher heavy particle temperature T_{hr} as well as electron concentration X_e near the axis indicating the existence of one or more types of reactions which are sensible to the selection of vibration-chemistry coupling model apart from the dissociation reactions. In order to find these reactions, we reran the simulations using Knab model with the coupling model of certain type of reactions replaced by Park model [45]. Figure 4.12 illustrates the results in terms of radial distributions of temperatures and electron mole fraction at the same location. As is presented in Figure 4.12, all types of reactions whose coupling model being replaced show a perfect agreement with the original one, except the charge exchange reactions which predict lower T_{hr} and X_e. We thus conclude that charge exchange reactions are responsible for the discrepancy between Knab and Treanor predictions as is illustrated in Figure 4.11 and their contribution to the chemical vibrational energy exchange should be carefully taken into account.

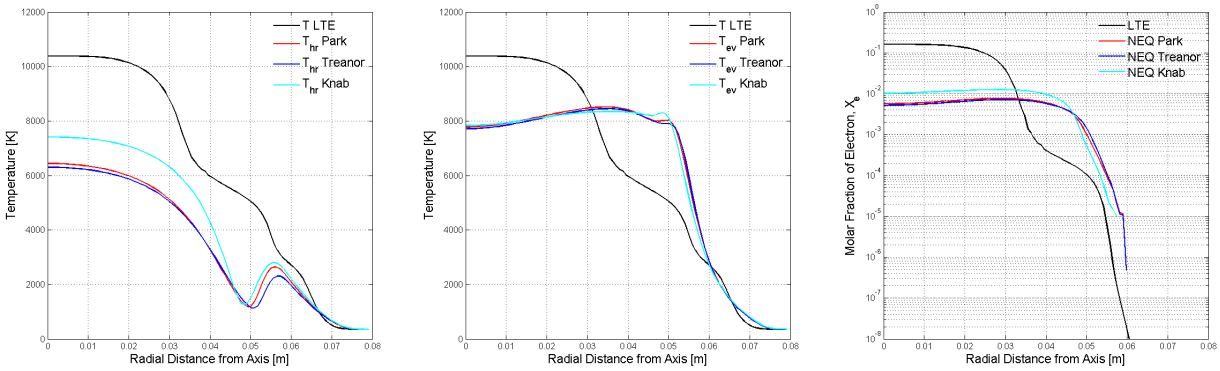

(a) T_{hr} (b) T_{ev} (c) X_e

Figure 4.11: Temperature and electron mole fraction profiles at midcoil ($z = 0.265\,m$) by different multi-temperature approaches.

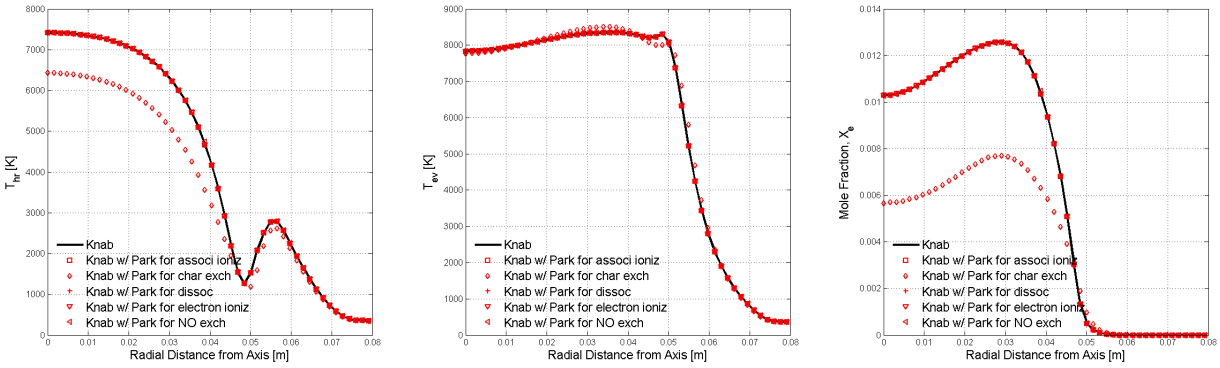

(a) T_{hr} (b) T_{ev} (c) X_e

Figure 4.12: Temperature and electron mole fraction profiles at midcoil ($z = 0.265\,m$) showing impact of chemical-thermal models on different reaction types.

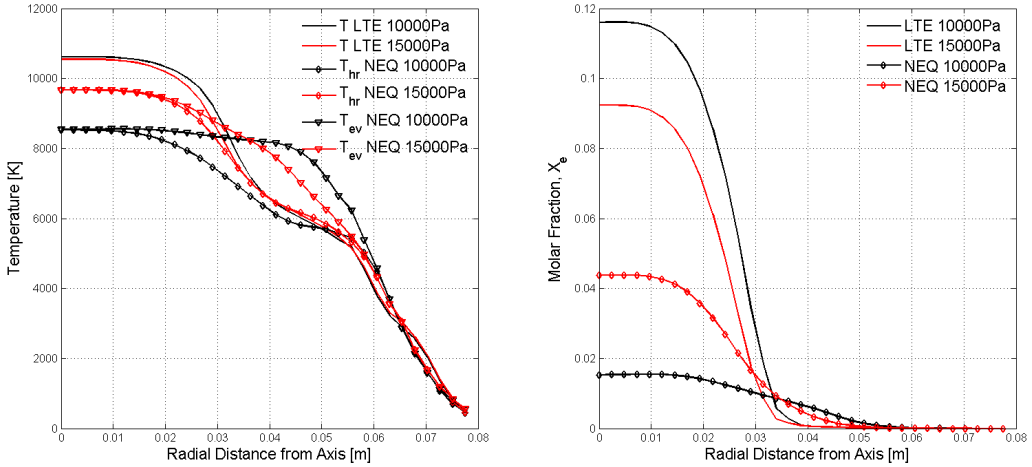

(a) Temperature profiles

(b) X_e

Figure 4.13: Temperature and electron mole fraction X_e at midcoil ($z = 0.265\,m$) with outlet pressures of $10000\,pa$ and $15000\,pa$.

4.4 Pressure Sensitivity Analysis

In this section we discuss how pressure affects thermal-chemical non-equilibrium. Comparison is made between $10000\,pa$ and $15000\,pa$. Here we adopt the operating conditions of Panesi et al. [43]: mass flow rate $Q = 8\,g/s$, frequency $f = 0.37\,MHz$ and input power $p = 80\,kW$. Figure 4.13 and 4.14 compare the radial distributions of temperatures and electron mole fraction given by varying outlet pressures ($10000\,pa$ and $15000\,pa$) at the mid-coil and outlet, respectively. As expected, when the pressure is raised non-equilibrium effects decrease and the difference between results obtained by TCNEQ and LTE formulations becomes less discernible. At mid-coil location, the $15000\,pa$ case still predicts higher T_{ev} although the thermal non-equilibrium region is narrower than the lower pressure case. At the outlet, T_{hr} and T_{ev} are finally equilibrated and reach a value closer to T given by LTE formulation, especially for the $15000\,pa$ case, indicating that LTE formulation is sufficient to predict outlet conditions at higher outlet pressures. The electron mole fraction X_e predicted by LTE formulation rises as pressure is lowered since the three-body recombination reactions are highly unlikely for diluted plasma.

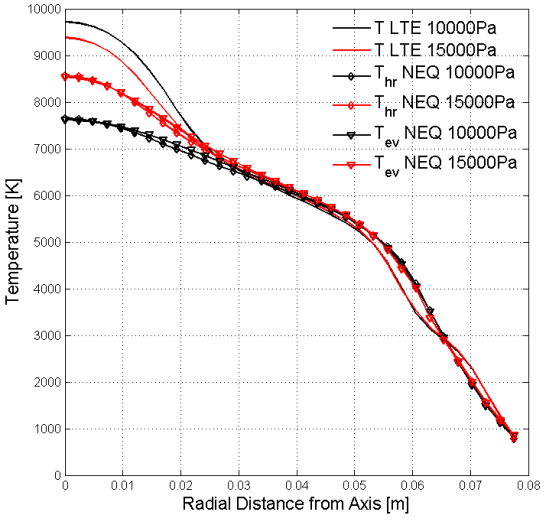

(a) Temperature profiles

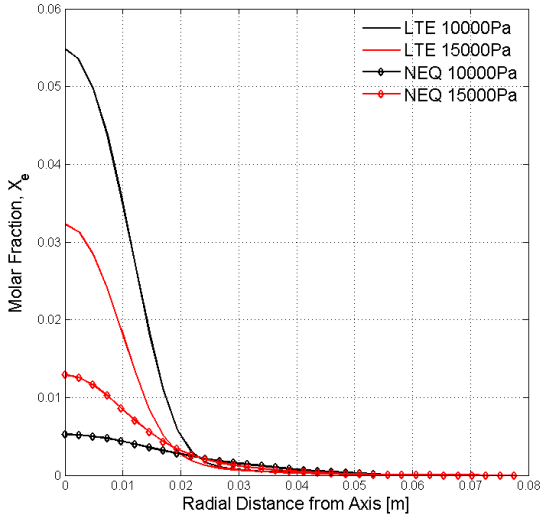

(b) X_e

Figure 4.14: Temperature and electron mole fraction X_e at outlet ($z = 0.470\,m$) with outlet pressures of $10000\,pa$ and $15000\,pa$.

Chapter 5

Conclusions and Future Work

In this work, we have analyzed non-equilibrium effects in plasma flows generated within VKI Plasmatron for four operating pressures ranging from 3 to 15 kPa. To this end, different models for the chemical kinetics and vibration-chemistry-vibration coupling have been integrated into numerical simulations and their effects on the flow and electrical fields have been compared. In addition, four finite-rate models have been used to obtain the non-equilibrium results. The analysis of these results leads us to the following conclusions:

- For the low-pressure cases, we observe a significant influence of the finite-rate chemistry model on the prediction of the flow behavior within the torch.
- From the comparison of the equilibrium and the non-equilibrium results, we notice that the flow in the torch is indeed in non-equilibrium for the low-pressure case. The degree of non-equilibrium depends on the position, decreases as we move toward the exit of the torch.
- As pressure rises, the differences between the predictions obtained with the two finite-rate models sharply decrease in the entire flow-field and consistently approach LTE conditions.
- The choice of the kinetic mechanism, and the coupling between kinetics and thermal relaxation appear to have a significant effect on the extent of non-equilibrium.

References

[1] D. Vanden Abeele. *An Efficient Computational Model for Inductively Coupled Air Plasma Flows under Thermal and Chemical Non-Equilibrium.* PhD thesis, Katholieke Universiteit Leuven, Chaussée de Waterloo, 72, 1640 Rhode-St-Genèse, Belgium, November 2000.

[2] B. Bottin, D. Vanden Abeele, M. Carbonaro, G. Degrez, and G. S. R. Sarma. Thermodynamic and transport properties for inductive plasma modeling. *Journal of Thermophysics and Heat Transfer*, 13:343–350, 1999.

[3] B. Bottin, D. Vanden Abeele, M. Carbonaro, G. Degrez, and G. S. R. Sarma. Thermodynamic and transport properties for inductive plasma modeling. *Journal of Thermophysics and Heat Transfer*, 13(3):343–350, 1999.

[4] M. I. Boulos. Flow and temperature fields in the fire-ball of an inductively coupled plasma. *IEEE Trans. Plasm. Sci.*, PS-4(1):28–39, 1976.

[5] J. D. Bukowski, D. B. Graves, and P. Vitello. Two-dimensional model of an inductively coupled plasma with comparison to experimental spatial profiles. *Journal of Applied Physics*, 80(5):2614–2623, 1996.

[6] G. Candler and I. Nompelis. Computational fluid dynamics for atmospheric entry. *RTO-EN-AVT-162 VKI lecture series*, 1(1), 2008.

[7] G. V. Candler and MacCormack. Computation of weakly ionized hypersonic flows in thermochemical nonequilibrium. *Journal of Thermophysics and Heat Transfer*, 5(11):266, 1991.

[8] M. L. Da Silva, V. Guerra, and J. Loureiro. Two-temperature models for nitrogen dissociation. *Chemical Physics*, 342:275–287, 2007.

[9] G. Degrez, A. Lani, M. Panesi, O. Chazot, and H. Deconinck. Modelling of high-enthalpy, high-mach number flows. *J. Phys. D: App. Phys*, 41, 2009.

[10] R. S. Devoto. Simplified expressions for the transport properties of ionized monoatomic gases. *Physics of Fluids*, 10(10):2105–2112, 1967.

[11] M. G. Dunn and S. W. Kang. Theoretical and experimental studies of reentry plasmas. NASA NTRS CR-2232, NASA, 1973.

[12] J. H. Ferziger and H. G. Kaper. *Mathematical Theory of Transport Processes in Gases.* North-Holland, Amsterdam, 1972.

[13] P. A. Gnoffo. *Annu. Rev. Fluid Mech.*, 31:459–494, 1999.

[14] P. A. Gnoffo, R. N. Gupta, and J. L. Shinn. *NASA STI/Recon Technical Report*, 89:16115, February 1989.

[15] P. Hammerling, J. D. Teare, and B. Kivel. Theory of Radiation from Luminous Shock Waves in Nitrogen. *Physics of Fluids*, 2:422–426, 1959.

[16] J. O. Hirschfelder, C. F. Curtiss, and R. B. Bird. *Molecular theory of gases and liquids.* John Wiley and Sons, New York, 1954.

[17] O. Knab, H. Freuhauf, and E. Messerschmid. Theory and validation of the physically consistent coupled vibration-chemistry-vibration model. *Journal of Thermophysics and Heat Transfer*, 9(2):219–226, 1995.

[18] D. Knight, J. Longo, D. Drikakis, D. Gaitonde, and A. Lani et al. Assessment of cfd capability for prediction of hypersonic shock interactions. *Prog. Aerosp. Sci.*, 48-49:8–26, 2012.

[19] A. F. Kolesnikov. Combined measurements and computations of high enthalpy and plasma flows for determination of TPM surface catalycity. NATO RTO-EN 8, von Karman Institute for Fluid Dynamics, St.-Genesius-Rode, Belgium, October 1999.

[20] A. F. Kolesnikov. Combined measurements and computations of high enthalpy and plasma flows for determination TPM surface catalycity. In *Measurements Techniques for High Enthalpy and Plasma Flows*, pages 8A 1–16, Rhode-St-Genèse Belgium, October 25-29 1999.

[21] A. F. Kolesnikov. Extrapolation from high enthalpy tests to flight based on the concept of local heat transfer simulation concept. In *Measurements Techniques for High Enthalpy and Plasma Flows*, pages 8B 1–14, Rhode-St-Genèse Belgium, October 25-29 1999. VKI-LS.

[22] A.F. Kolesnikov. Aerothermodynamic simulation in sub- and supersonic high-enthalpy jets: experiment and theory. In *ESA SP-367*. ESTEC, Noordwijk, the Netherlands, 1994.

[23] A. Lani, J. Garicano Mena, and H. Deconick. A residual distribution method for symmetrized systems in thermochemical nonequilibrium. In *AIAA-2011-3546*, Honolulu (Hawaii), Jun 2011. 20th AIAA CFD Conference.

[24] A. Lani, T. Quintino, D. Kimpe, H. Deconinck, S. Vandewalle, and S. Poedts. The COOLFluiD framework: Design solutions for high-performance object oriented scientific computing software. In P. M. A. Sloot V. S. Sunderan, G. D. van Albada and J. J. Dongarra, editors, *Computational Science ICCS 2005*, volume 1 of *LNCS 3514*, pages 281–286, Atlanta, GA, USA, May 2005. Emory University, Springer.

[25] A. Lani, P. Duarte Santos, and A. Sanna. An efficient monte carlo method for radiation transport in aerothermo-dynamic simulations. In *AIAA 2013-2893*, San Diego (CA), Jun 2013. 44th AIAA Thermophysics Conference.

[26] A. Lani, N. Villedieu, K. Bensassi, L. Kapa, M. Vymazal, M. S. Yalim, and M. Panesi. Coolfluid: an open computational platform for multi-physics simulation and research. In *AIAA 2013-2589*, San Diego (CA), Jun 2013. 21th AIAA CFD Conference.

[27] M. S. Liou. A sequel to ausm, part ii: Ausm$^+$-up for all speeds. *Journal of Computational Physics*, 214:137–170, 2006.

[28] Meng-Sing Liou. A sequel to ausm: Ausm¡ sup¿+¡/sup¿. *Journal of computational Physics*, 129(2):364–382, 1996.

[29] Meng-Sing Liou and Christopher J Steffen Jr. A new flux splitting scheme. *Journal of Computational physics*, 107(1):23–39, 1993.

[30] T. Magin. *A Model for Inductive Plasma Wind Tunnels*. PhD thesis, von Karman Institute for Fluid Dynamics, Rhode-St-Genese, Belgium, June 2004.

[31] T. Magin and G. Degrez. Transport algorithms for partially ionized and unmagnetized plasmas. *Journal of Computational Physics*, 198:424, 2004.

[32] Thierry E. Magin and Gérard Degrez. Transport properties of partially ionized and unmagnetized plasmas. *Phys. Rev. E*, 70:046412, Oct 2004.

[33] P. Marrone and C. Treanor. Chemical relaxation with preferential dissociation from excited vibrational levels. *The Physics of Fluids*, 6:1215–1221, 1963.

[34] J.W. McKelliget. A mathematical model of an inductive plasma torch. Technical Report 86-112.1, University of Lowell, College of Engineering, September 1986.

[35] J. Mostaghimi, P. Proulx, and M. I. Boulos. An analysis of the computer modeling of the flow and temperature fields in an inductively coupled plasma. *J. Numer. Heat Transf.*, 8:187–201, 1985.

[36] A. Munafo, A. Lani, A. Bultel, and M. Panesi. Modeling of non-equilibrium phenomena in expanding flows by means of a collisional-radiative model. *Physics of Plasma*, 20(7), 2013.

[37] A. Munafò, M. Panesi, and T. E. Magin. *Phys. Rev. E*, 23(2):023001, February 2014.

[38] Munafò, A., Panesi, M., Jaffe, R.L., Colonna, G., and Magin, T.E. *Eur. Phys. J. D*, 66(7):188, 2012.

[39] M. Panesi, R. L. Jaffe, D. Schwenke, and E. T. Magin. Rovibrational internal energy transfer and dissociation of n_2n system in hypersonic flows. *Journal of Chemical Physics*, 138:044312, 2013.

[40] M. Panesi and A. Lani. Collisional radiative coarse-grain model for ionization in air. *Physics of Fluids*, 25:057101 (27pp), 2013.

[41] M. Panesi, T. Magin, A. Bourdon, A. Bultel, and O. Chazot. Analysis of the Fire II flight experiment by means of a collisional radiative model. *Journal of Thermophysics and Heat Transfer*, 23(2):236–248, April-June 2009.

[42] M. Panesi, T. Magin, A. Bourdon, A. Bultel, and O. Chazot. Study of electronically excited state populations of atoms and molecules predicted by means of a collisional-radiative model for the fire ii flight experiment. *Journal of Thermophysics and Heat Transfer*, 25(25):361–374, 2011.

[43] M. Panesi, P. Rini, G. Degrez, and O. Chazot. Analysis of chemical non-equilibrium and elemental demixing in the VKI plasmatron. *Journal Thermophysics and Heat Transfer*, 21(1):57–66, 2007.

[44] C. Park. *Nonequilibrium Hypersonic Aerothermodynamics.* John Wiley and Sons, New York, 1989.

[45] C. Park. Review of chemical-kinetic problems of future NASA missions, I: Earth entries. *Journal of Thermophysics and Heat Transfer*, 7(3):385–398, 1993.

[46] C. Park, R.L. Jaffe, and H. Partridge. Chemical-kinetic parameters of hyperbolic Earth entry. *Journal of Thermophysics and Heat Transfer*, 15(1):76, 2001.

[47] P. Rini. *Analysis of differential diffusion phenomena in high enthalpy flows.* PhD thesis, von Karman Institute for Fluid Dynamics, Rhode-St-Genese, Belgium, March 2006.

[48] D. Vanden Abeele. *An Efficient Computational Model for Inductively Coupled Air Plasma Flows under Thermal and Chemical Non-Equilibrium.* PhD thesis, von Karman Institute, Rhode-Saint-Genèse, Belgium, 2000.

[49] W.G. Vincenti and C.H. Kruger. *Introduction to Physical Gas Dynamics.* John Wiley and Sons, New York, 1965.

[50] M. S. Yalim, D. V. Abeele, A. Lani, T. Quintino, and H. Deconinck. A finite volume implicit time integration method for solving the equations of ideal magnetohydrodynamics for the hyperbolic divergence cleaning approach. *JCP*, 230(15):6136–6154, Jul 2011.

[51] J. M. Yos. Approximate equations for the viscosity and translational thermal conductivity of gas mixtures. Contract Report AVSSD-0112-67-RM, Avco Corporation, Wilmington, Massachusetts, April 1967.